



**HAL**  
open science

## Cross-comparison of global simulation models applied to Mercury's dayside magnetosphere

Sae Aizawa, Léa S Griton, Shahab Fatemi, Willi Exner, Jan Deca, Filippo Pantellini, Manabu Yagi, Daniel Heyner, Vincent Génot, Nicolas André, et al.

► **To cite this version:**

Sae Aizawa, Léa S Griton, Shahab Fatemi, Willi Exner, Jan Deca, et al.. Cross-comparison of global simulation models applied to Mercury's dayside magnetosphere. *Planetary and Space Science*, 2021, 198 (April), pp.105176. 10.1016/j.pss.2021.105176 . hal-02551111v3

**HAL Id: hal-02551111**

**<https://hal.science/hal-02551111v3>**

Submitted on 2 Feb 2021

**HAL** is a multi-disciplinary open access archive for the deposit and dissemination of scientific research documents, whether they are published or not. The documents may come from teaching and research institutions in France or abroad, or from public or private research centers.

L'archive ouverte pluridisciplinaire **HAL**, est destinée au dépôt et à la diffusion de documents scientifiques de niveau recherche, publiés ou non, émanant des établissements d'enseignement et de recherche français ou étrangers, des laboratoires publics ou privés.



Distributed under a Creative Commons Attribution - NonCommercial 4.0 International License

# Journal Pre-proof

Cross-comparison of global simulation models applied to Mercury's dayside magnetosphere

S. Aizawa, L.S. Griton, S. Fatemi, W. Exner, J. Deca, F. Pantellini, M. Yagi, D. Heyner, V. Génot, N. André, J. Amaya, G. Murakami, L. Beigbeder, M. Gangloff, M. Bouchemit, E. Budnik, H. Usui

PII: S0032-0633(21)00015-5

DOI: <https://doi.org/10.1016/j.pss.2021.105176>

Reference: PSS 105176

To appear in: *Planetary and Space Science*

Received Date: 5 June 2020

Revised Date: 23 November 2020

Accepted Date: 27 January 2021

Please cite this article as: Aizawa, S., Griton, L.S., Fatemi, S., Exner, W., Deca, J., Pantellini, F., Yagi, M., Heyner, D., Génot, V., André, N., Amaya, J., Murakami, G., Beigbeder, L., Gangloff, M., Bouchemit, M., Budnik, E., Usui, H., Cross-comparison of global simulation models applied to Mercury's dayside magnetosphere, *Planetary and Space Science*, <https://doi.org/10.1016/j.pss.2021.105176>.

This is a PDF file of an article that has undergone enhancements after acceptance, such as the addition of a cover page and metadata, and formatting for readability, but it is not yet the definitive version of record. This version will undergo additional copyediting, typesetting and review before it is published in its final form, but we are providing this version to give early visibility of the article. Please note that, during the production process, errors may be discovered which could affect the content, and all legal disclaimers that apply to the journal pertain.

© 2021 Published by Elsevier Ltd.



1 **Author statement for the paper :**

2 **Cross-comparison of global simulation models applied to**  
 3 **Mercury's dayside magnetosphere**

4 S. Aizawa<sup>a,b,\*</sup>, L. S. Griton<sup>a,k</sup>, S. Fatemi<sup>c,d</sup>, W. Exner<sup>e,f,g</sup>, J. Deca<sup>h,i,j</sup>, F. Pantellini<sup>k</sup>, M. Yagi<sup>l</sup>, D.  
 5 Heyner<sup>e</sup>, V. Génot<sup>a</sup>, N. André<sup>a</sup>, J. Amaya<sup>m</sup>, G. Murakami<sup>n</sup>, L. Beigbeder<sup>o</sup>, M. Gangloff<sup>a</sup>, M.  
 6 Bouchemit<sup>a</sup>, E. Budnik<sup>p</sup>, H. Usui<sup>q</sup>

7 <sup>a</sup>IRAP, CNRS-CNES-UPS, Toulouse, France

8 <sup>b</sup>Graduate School of Science, Tohoku University, Sendai, Japan

9 <sup>c</sup>Swedish Institute of Space Physics, Kiruna, Sweden

10 <sup>d</sup>Department of Physics at Umeå University, Umeå, Sweden

11 <sup>e</sup>Institute for Geophysics and extraterrestrial Physics, Technische Universität Braunschweig,  
 12 Braunschweig, Germany

13 <sup>f</sup>Institute for Theoretical Physics, Technische Universität Braunschweig, Braunschweig, Germany

14 <sup>g</sup>School of Earth and Atmospheric Sciences, Georgia Institute of Technology, Atlanta, USA

15 <sup>h</sup>Laboratory for Atmospheric and Space Physics (LASP), University of Colorado Boulder, Boulder, Colorado  
 16 80303, USA

17 <sup>i</sup>Institute for Modeling Plasma, Atmospheres and Cosmic Dust, NASA/SSERVI, California 94035, USA

18 <sup>j</sup>Laboratoire Atmosphères, Milieux, Observations Spatiales (LATMOS), Université de Versailles `a Saint  
 19 Quentin, 78280 Guyancourt, France

20 <sup>k</sup>LESIA, Observatoire de Paris, Université PSL, CNRS, Sorbonne Université, Université de Paris, 5 place  
 21 Jules Janssen, 92195 Meudon, France

22 <sup>l</sup>RIKEN, Kobe, Japan

23 <sup>m</sup>CmPA, Mathematics Department, KU Leuven, Belgium

24 <sup>n</sup>ISAS/JAXA, Sagami-hara, Japan

25 <sup>o</sup>GFI, Toulouse, France

26 <sup>p</sup>Noveltis, Toulouse, France

27 <sup>q</sup>Kobe University, Kobe, Japan

28

29 **Sae AIZAWA: Conceptualization, Visualization, writing-original draft preparation,**  
 30 **writing – review & editing**

31 **Lea S. Griton : Conceptualization, Methodology, validation, writing-original draft**  
 32 **preparation, writing – review & editing**

33 **S. Fatemi: Conceptualization, Methodology, validation, writing-original draft**  
 34 **preparation, writing – review & editing**

35 **W. Exner : Conceptualization, Methodology, validation, writing-original draft**  
 36 **preparation, writing – review & editing**

37 **J. Deca : writing-original draft preparation, writing – review & editing**

38 **F. Pantellini : Methodology, validation, writing-original draft preparation, writing –**  
 39 **review & editing**

40 **M. Yagi: Methodology, writing-original draft preparation, writing – review & editing**

- 41
- 42 **D. Heyner: Supervision, writing – review & editing**
- 43 **V. Génot: writing – review & editing, Methodology**
- 44 **N. André: writing – review & editing, funding acquisition**
- 45 **J. Amaya : writing-original draft preparation**
- 46 **G. Murakami : Supervision**
- 47 **H. Usui: Supervision**
- 48 **L. Beigbeder, M. Gangloff, M. Bouchemit, E. Budnik : Technical support on**
- 49 **Methodology**
- 50

# Cross-comparison of global simulation models applied to Mercury's dayside magnetosphere

S. Aizawa<sup>a,b,\*</sup>, L. S. Griton<sup>a,k</sup>, S. Fatemi<sup>c,d</sup>, W. Exner<sup>e,f,g</sup>, J. Deca<sup>h,i,j</sup>, F. Pantellini<sup>k</sup>, M. Yagi<sup>l</sup>, D. Heyner<sup>e</sup>, V. Génot<sup>a</sup>, N. André<sup>a</sup>, J. Amaya<sup>m</sup>, G. Murakami<sup>n</sup>, L. Beigbeder<sup>o</sup>, M. Gangloff<sup>a</sup>, M. Bouchemit<sup>a</sup>, E. Budnik<sup>p</sup>, H. Usui<sup>q</sup>

<sup>a</sup>*IRAP, CNRS-CNES-UPS, Toulouse, France*

<sup>b</sup>*Graduate School of Science, Tohoku University, Sendai, Japan*

<sup>c</sup>*Swedish Institute of Space Physics, Kiruna, Sweden*

<sup>d</sup>*Department of Physics at Umeå University, Umeå, Sweden*

<sup>e</sup>*Institute for Geophysics and extraterrestrial Physics, Technische Universität Braunschweig, Braunschweig, Germany*

<sup>f</sup>*Institute for Theoretical Physics, Technische Universität Braunschweig, Braunschweig, Germany*

<sup>g</sup>*School of Earth and Atmospheric Sciences, Georgia Institute of Technology, Atlanta, USA*

<sup>h</sup>*Laboratory for Atmospheric and Space Physics (LASP), University of Colorado Boulder, Boulder, Colorado 80303, USA*

<sup>i</sup>*Institute for Modeling Plasma, Atmospheres and Cosmic Dust, NASA/SSERVI, California 94035, USA*

<sup>j</sup>*Laboratoire Atmosphères, Milieux, Observations Spatiales (LATMOS), Université de Versailles à Saint Quentin, 78280 Guyancourt, France*

<sup>k</sup>*LESIA, Observatoire de Paris, Université PSL, CNRS, Sorbonne Université, Université de Paris, 5 place Jules Janssen, 92195 Meudon, France*

<sup>l</sup>*RIKEN, Kobe, Japan*

<sup>m</sup>*CmPA, Mathematics Department, KU Leuven, Belgium*

<sup>n</sup>*ISAS/JAXA, Sagami, Japan*

<sup>o</sup>*GFI, Toulouse, France*

<sup>p</sup>*Noveltis, Toulouse, France*

<sup>q</sup>*Kobe University, Kobe, Japan*

---

## Abstract

We present the first comparison of multiple global simulations of the so-

---

\*Corresponding author.

*Email address:* sae.aizawa@irap.omp.eu (S. Aizawa)

lar wind interaction with Mercury’s dayside magnetosphere, conducted in the framework of the international collaborative project SHOTS - Studies on Hermean magnetosphere Oriented Theories and Simulations. Two 3D magnetohydrodynamic and two 3D hybrid simulation codes are used to investigate the global response of the Hermean magnetosphere without its exosphere to a northward-oriented interplanetary magnetic field. We cross-compare the results of the four codes for a theoretical case and a MESSENGER orbit with similar upstream plasma conditions. The models agree on bowshock and magnetopause locations at  $2.1 \pm 0.1$  and  $1.4 \pm 0.08$  Mercury planetary radii, respectively. The latter locations may be influenced by subtle differences in the treatment of the plasma boundary at the planetary surface. The predicted magnetosheath thickness varies less between the codes. Finally, we also sample the plasma data along virtual trajectories of BepiColombo’s Magnetospheric and Planetary Orbiter. Our ability to accurately predict the structure of the Hermean magnetosphere aids the analysis of the onboard plasma measurements of past and future magnetospheric missions.

*Keywords:* Mercury, BepiColombo, Modeling

---

## 1. Introduction

Mercury is a planet of extremes that is continuously battered by a harsh and dynamic solar wind. Combined with interplanetary magnetic field (IMF) magnitudes up to 30 nT and a small Parker spiral angle, Mercury’s weak internal magnetic field produces a unique magnetosphere in the solar system [1, 2, 3, 4, 5]. For example, the Hermean magnetosphere is twenty times smaller in volume than Earth’s magnetosphere and Mercury’s volume frac-

8 tion in its magnetosphere is approximately five hundred times larger than  
9 the equivalent terrestrial number Slavin et al. [6], Slavin et al. [7, 8]. As a  
10 result, the solar wind can directly interact with the surface, even outside the  
11 magnetospheric cusps [9]. In addition, the significant offset between the mag-  
12 netic dipole origin and the center of the planet results in a surface magnetic  
13 field strength in the northern hemisphere that is double the nominal value  
14 estimated for the southern hemisphere [10, 11, 12, 13]. These particularities  
15 culminate in fascinating particle precipitation patterns and differential space  
16 weathering that is as variable as the upstream solar wind [14, 15, 16]. The  
17 absence of a significant ionosphere makes Mercury’s conductive core an inte-  
18 gral part of the electrodynamic current closure and complicates the evolution  
19 of the complex local plasma environment even more [17, 18].

20  
21 Numerical simulations of the solar wind interaction with the Hermean  
22 magnetosphere have thus far adopted multi-fluid/magnetohydrodynamic [19,  
23 20, 17, 21] and hybrid approaches (representing the ions as computational  
24 particles and the electron populations as a (massless) fluid) [22, 23, 24, 25, 26,  
25 27, 28, 29, 30, 31, 32, 16, 33]. These models, designed to focus on the ion ki-  
26 netics, have been successful in recreating the general structure of Mercury’s  
27 local plasma environment. For example, with a 3D hybrid model, Müller  
28 et al. [34] characterised a diamagnetic current system that originates from the  
29 proton pressure gradients at Mercury’s inner magnetosphere to explain the  
30 day- and night-side diamagnetic decreases observed by MESSENGER [6, 35].  
31 In addition, recent numerical developments have produced the first fully ki-  
32 netic, global simulations of the Hermean magnetosphere [36, 37, 38].

33

34 Due to mission constraints such as limited field of view and energy range  
35 to detect ions, both the Mariner-10 and MESSENGER spacecraft were lim-  
36 ited to measure the Hermean plasma environment and thus, to fully disen-  
37 tangle plasma processes such as finite-gyroradius effects and complex elec-  
38 tron dynamics [4]. Complementary to the previous missions, BepiColombo's  
39 Magnetospheric (Mio) [39]) and Planetary Orbiter (MPO) [40]) allow for  
40 multi-spacecraft coordinated observations [41]. Their plasma instruments  
41 focus on direct measurements of the response of Mercury's magnetosphere  
42 and its near-space environment to dynamic changes in the solar wind, in-  
43 cluding plasma-wave-charged-particle resonances, kinetic-scale instabilities  
44 and particle distributions, and energy transfer via field-aligned currents and  
45 waves [4].

46

47 In order to optimally prepare for the measurement campaign and to be  
48 able to fully interpret and analyse the data during the forthcoming Mercury  
49 flybys and during the orbital phase, or in other words, to exploit most effi-  
50 ciently the multi-point measurements allowed by the dual spacecraft and the  
51 synergies between the various sensors of the onboard plasma suite, sophis-  
52 ticated modelling tools are required. Hence, the SHOTS (Studies on Her-  
53 mean magnetosphere Oriented Theories and Simulations) project has been  
54 established as an integral part of the BepiColombo Young Scientist Working  
55 Group. Its aim is to share and compare simulations results among the Bepi-  
56 Colombo Science Working Team in order to prepare the scientific analysis of  
57 the in-situ magnetospheric observations gathered by Mio and MPO.



58

59 In this first comparative study, we identify the differences between fluid  
60 and hybrid simulation approaches to model the structure of the Hermean  
61 magnetosphere and its plasma environment. We compare the bow shock  
62 and magnetopause locations with a representative set of MESSENGER mea-  
63 surements and predict the plasma environment along virtual trajectories of  
64 BepiColombo's Mio and MPO spacecraft.

65

## 66 **2. Model descriptions and methodology constraints**

67 The four computer models used in this comparison study are briefly de-  
68 scribed here, with special emphasis on their inner boundary conditions. We  
69 find that subtle differences in the treatment of the plasma boundary at the  
70 planetary surface affect the global solar wind - magnetosphere structure. Two  
71 magnetohydrodynamic (MHD) and two hybrid codes have been employed to  
72 identify the consequences of the different assumptions that are implemented  
73 in the physical model of the codes. In Table 1, we summarize the general  
74 numerical settings adopted for the four codes, such as the number of cells  
75 used, the size of the simulation domain, the spatial resolution, and the time  
76 step. The output from all models are stored and discussed using the Mer-  
77 cury Solar Orbital (MSO) frame. The X-axis points towards the Sun and  
78 the Y-axis is chosen opposite to the orbital motion of Mercury. The Z-axis  
79 points to the geophysical north and completes the right-handed coordinate  
80 system. The intrinsic magnetic field of the planet is set as a dipole with a  
81 480 km offset towards the north from the planetary center [42]. The dipole

82 moment is  $200 \text{ nT} \times R_M^3$ . To avoid further numerical complexities, we do not  
 83 include the tenuous Mercury’s exosphere in our simulations just yet. In a  
 84 recent hybrid study, Exner et al. [33] investigated the kinetic effects of dif-  
 85 ferent sodium exosphere surface densities onto the Hermean magnetsphere.  
 86 Authors found that an average sodium exosphere based on a realistic model  
 87 of [cite Gamborino Monte-Carlo Paper] does not pose a significant factor to  
 88 the magnetic field structure inside the magnetosphere. Therefore, we do not  
 89 include the tenuous sodium exosphere in this study.

90

### 91 2.1. MHD models

92 The three-dimensional MPI-AMRVAC (MPI-Adaptive Mesh Refinement  
 93 Versatile Advection Code) code (hereafter AMRVAC) is the first three-dimensional  
 94 MHD model we use in this study. This code integrates the MHD equations  
 95 using a two-step Lax-Friedrichs-type scheme associated with a Woodward  
 96 gradient limiter [43, 44]. A Powell correction is also used to satisfy the  
 97  $\nabla \cdot \mathbf{B} = 0$  condition at each time step [45]. In order to limit magnetic diffu-  
 98 sion, the magnetic field  $\mathbf{B}$  is split into an analytically prescribed background  
 99 field  $\mathbf{B}_0$  and a residual field  $\mathbf{B}_1$  [46]. The full system of equations is solved  
 100 on a spherical grid that is linearly spaced along the angular coordinates  $\theta$   
 101 and  $\phi$  and logarithmically spaced along the radial coordinate  $r$ . Hence, the  
 102 simulation domain itself is a spherical shell. Note from Table 1 that only  
 103 AMRVAC employs a spherical coordinate system. With a total number of  
 104 cells of  $(N_r, N_\theta, N_\phi) = (36, 36, 72)$ , covering the radial interval  $r \in R_M [1, 10]$ ,  
 105 the horizontal and vertical cell size near the surface are 213 km and 161 km,  
 106 respectively. At the outer boundary, free slip conditions ( $\partial/\partial r = 0$ ) are ap-

107 plied to all fields where the angle between the solar wind direction and the  
 108 normal to the boundary direction is  $< 80^\circ$ . Ambient (upstream) solar wind  
 109 conditions are set at the remaining sides of the domain. At the inner bound-  
 110 ary of the simulation domain, here the planetary surface, the radial velocity  
 111 is set to zero. A free slip condition is applied to the tangential components  
 112 of the momentum  $\rho\mathbf{v}$ . If the radial velocity immediately above the surface  
 113 is positive (i.e. in case of outflow), the plasma number density and the total  
 114 fluid pressure are set to  $n = 30 \text{ cm}^{-3}$  and  $p = 0.1 \text{ nPa}$ , respectively. On the  
 115 other hand, if the radial velocity immediately above the surface is negative  
 116 (i.e. in case of inflow),  $n$  and  $p$  are allowed to evolve within  $15 - 150 \text{ cm}^{-3}$  and  
 117  $0.1 - 1 \text{ nPa}$ . A free slip condition is also applied to the normal component of  
 118  $\mathbf{B}_1$  at the surface. The tangential components are set to zero. The results  
 119 of AMRVAC are interpolated to a uniform Cartesian grid with a spatial res-  
 120 olution of  $81.5^3 \text{ km}^3$  for ease of comparison with the other simulation models.

121

122 Yagi's code is the second three-dimensional MHD model we use [47, 48].  
 123 In this code, a Rational-CIP (Constrained Interpolation Profile) algorithm  
 124 is implemented to solve the advection term [48] and a fourth-order Runge-  
 125 Kutta and a fourth-order central difference method are used to solve the  
 126 non-advection terms needed to advance the numerical scheme in time and  
 127 space. In contrast to AMRVAC, the magnetic vector potential  $\mathbf{A}$  is com-  
 128 puted instead of the magnetic field, ensuring  $\nabla \cdot \mathbf{B} = 0$  by definition and a  
 129 uniform Cartesian grid is adopted. In this study, the grid resolution is set  
 130 to  $122 \text{ km}^3$ . The simulation domain measures  $(-10 : +6, \pm 5, \pm 5) R_M$ , with  
 131 the number of cells of  $(Lx, Ly, Lz) = (300, 300, 300)$ . The inner boundary of

132 the computational domain is the planetary surface. Mercury is treated as a  
 133 reflective obstacle, allowing no flux to penetrate across the surface (obsta-  
 134 cle). We also apply the free slip condition which does not allow any radial  
 135 pressure and density gradient at the planetary surface. The inner boundary  
 136 conditions accommodate a smooth convection of the magnetic field in the  
 137 vicinity of the planet, mimicking obstacle with low conductivity.

138

### 139 *2.2. Hybrid models*

140 AIKEF (Adaptive Ion Kinetic Electron Fluid) is the first three-dimensional  
 141 hybrid model we employ in this study. Contrary to MHD, a hybrid model  
 142 treats ions kinetically while electrons are included as a massless charge-  
 143 neutralizing fluid. In this study, the number of computational macro-particle  
 144 per cell is set to 25 to represent their Maxwellian velocity distribution. The  
 145 magnetic and electric fields are obtained by solving the Maxwell equations,  
 146 i.e., the electric field  $\mathbf{E}$  is directly calculated from the electron momentum  
 147 equation and Faraday's law,  $\partial\mathbf{B}/\partial t = -\nabla \times \mathbf{E}$ , is used to advance the mag-  
 148 netic field  $\mathbf{B}$  in time. The fields propagate between the grid points with  
 149 a Runge-Kutta-algorithm. AIKEF operates on a Cartesian grid and the  
 150 mesh is capable of automatically adapting its resolution in regions where  
 151 large field gradients exist [49, 32]. For simplicity, we do not activate this  
 152 function here and use a fixed spatial resolution of  $100 \text{ km}^3$  instead, and the  
 153 simulation domain is set to  $(-6 : +8, \pm 9, \pm 9) R_M$  with the number of cells  
 154 of  $(Lx, Ly, Lz) = (320, 224, 224)$ . To include magnetic induction processes  
 155 within Mercury, Mercury's core is assumed to be highly conductive leading  
 156 the resistivity in the core region is set to zero. The magnetic diffusion in the

157 mantle is facilitated by applying a maximum resistivity of  $1.21 \cdot 10^7 \Omega \cdot m$   
 158 [17, 32] and employing a Crank-Nicolson algorithm. The resistivity profile  
 159 is smoothed at the surface and core-mantle-boundary, identical to Jia et al.  
 160 [17]. Mercury’s surface is treated as a perfect plasma absorber, i.e., particles  
 161 impacting the surface are removed. To ensure numerical stability, 0.2% of  
 162 smoothing parameter is applied between the grid points [50].

163

164 The Amitis is a GPU-based (Graphics Processing Units) three-dimensional  
 165 hybrid model of plasma that currently runs only on a single CPU-GPU  
 166 pair [30]. It has been developed to reduce the computational resources that  
 167 are typically needed for running global simulations and resulted in perfor-  
 168 mance enhancement of 10x-100x over its CPU-based predecessor. Identical  
 169 to AIKEF, the model kinetically tracks positively charged macro-particles,  
 170 i.e., the ion population, by solving the Lorentz equation of motion while us-  
 171 ing a fluid description for mass-less electrons. The electric field and magnetic  
 172 field are obtained by solving Maxwell equations. The model is grid-based and  
 173 uses regular-spaced, cell-center Cartesian grids to solve all the equations. We  
 174 choose a spatial resolution of  $125 \text{ km}^3$  with 16 macro-particles per cell, and  
 175 simulation domain is set to  $(\pm 7, \pm 10, \pm 10) R_M$ . The model self-consistently  
 176 couples the geophysical, induced electromagnetic response of the interior of  
 177 a planetary body to the electromagnetic response of the incident plasma and  
 178 magnetic fields by solving Maxwell’s equations for the plasma and a mag-  
 179 netic diffusion equation ( $\partial \mathbf{B} / \partial t = -\nabla \times \nabla \times \mathbf{B} / \mu_0 \sigma$ ) for the interior of the  
 180 object, where  $\mu_0$  is the permeability of free space and  $\sigma$  is the conductive  
 181 profile for the interior of the planetary body [30]. Amitis adopts periodic

182 outer boundary conditions for its particles and electromagnetic fields along  
183 the axes perpendicular to the solar wind flow. Parallel to the flow the code  
184 continuously injects solar wind ions at the most upstream grid cell. The  
185 downstream boundary, identical to its implementation of the planetary sur-  
186 face, is a perfect plasma absorber. Unlike AIKEF, a smoothing routine is  
187 not applied in Amitis.

188

189 When plasma impacts onto the surface, a vacuum is formed in the down-  
190 stream regions. In contrast to MHD codes where a minimum charge density  
191 is present in these regions of vacuums to enable the continued calculation  
192 of the field equations, hybrid models need special handlings of the vacuum  
193 regions. AIKEF employs ghost-ions with the same charge-to-mass ratio as  
194 solar wind ions but in tenuous densities to propagate the electric and mag-  
195 netic fields in the vacuum regions. This approach enables a smooth density  
196 profile at the vacuum region edges without large gradients, while also increas-  
197 ing the numerical resource usage due to the handling of an additional species  
198 Trávníček et al. [25]. A different approach is used in Amitis, where, each  
199 time step, the cells within the vacuum regions obtain a flat resistivity value.  
200 This approach allows for the emergence of localized currents that propagate  
201 the electric and magnetic fields instead of ions. The vacuum state of the cells  
202 is checked every time step which does not increase numerical resources by  
203 a significant amount. However, this approach leads to unphysical resistivity  
204 gradients throughout the downstream regions that might lead to unphysi-  
205 cal currents. Therefore, the resistivity value is capped at  $10^7 \Omega \text{m}$  so limit  
206 the resistivity gradients. As both approaches result in good agreement with

Table 1: Summary of the numerical settings. For AMRVAC the finest spatial resolution is quoted.

	Grid type	#cells	Domain size	Resolution	Time step	particles/cell
AMRVAC [43]	Spherical	(36, 36, 72)	$r \in R_M [1, 10]$	$213 \times 161$ km	0.03 sec	-
Yagi [47]	Cartesian	(300, 300, 300)	$(-10:+6,\pm 5,\pm 5) R_M$	122 km	0.02 sec	-
AIKEF [49]	Cartesian	(320, 224, 224)	$(-6:+8,\pm 9,\pm 9) R_M$	100 km	0.08 sec	25
Amitis [30]	Cartesian	(234, 396, 396)	$(\pm 7,\pm 10,\pm 10) R_M$	125 km	0.001 sec	16

207 spacecraft data [32, 31], we do not investigate how these approaches relate  
 208 to each other in this study.

### 209 2.3. Common visualization tools

210 We use netCDF as a multidimensional format with meta information for  
 211 all simulations. It allows us to have a unified format for comparative vi-  
 212 sualizations, data interoperability and reusability. In the present study, we  
 213 employ Paraview for 3D data visualization and analysis. In addition, we  
 214 use 3Dview and AMDA (Automated Multi-Dataset Analysis), which makes  
 215 use of the SPASE (Physics Archive Search and Extract) simulation data  
 216 model [51, 52, 53, 54]. Using SPICE kernels, 3Dview is a 3D JAVA tool that  
 217 provides visualizations of the positions and attitudes of planetary missions  
 218 and bodies in combination with observational data, simulations, and analyt-  
 219 ical models. AMDA is an online database and analysis tool in which in-situ  
 220 observations, ground based observations, and models can be browsed, manip-  
 221 ulated and downloaded (a workspace is available for each user). AMDA and  
 222 3Dview are developed by the CDPP (Centre de Données de la Physique des  
 223 Plasmas) and available to contributing developers under a GPLv3 licence.

### 224 3. Science cases

225 In this work we discuss two cases: (a) a classical textbook case under  
226 purely northward IMF conditions to obtain the characteristics of each code,  
227 and (b) a direct comparison with a pre-selected MESSENGER orbit.

228

#### 229 3.1. Case a: Northward IMF

230 Northward IMF conditions are chosen to anticipate a stable dayside mag-  
231 netosphere structure. Typically, a southward IMF gives rise to more unstable  
232 magnetosphere conditions as continuous dayside magnetic reconnection in  
233 combination with a relatively short Dungey cycle does not allow the system  
234 to relax [12]. In the case of a northward IMF, the reconnection sites move to  
235 high latitudes near the magnetospheric cusps.

236

237 We set the typical solar wind condition around 0.3 AU, e.g., IMF magni-  
238 tude to 20 nT and adopt a solar wind proton density of  $30 \text{ cm}^{-3}$ , an Alfvén  
239 Mach number of 5 and a total plasma beta ( $\beta$ ) of 1.3. The solar wind speed  
240 measures  $400 \text{ km s}^{-1}$  [55, 9]. The MHD models assume a total density equal to  
241 the proton density, whereas the plasma temperature (43 eV) is set to the sum  
242 of the electron (21.5 eV) and proton (21.5 eV) temperatures (Table 2) [56, 57].

243

#### 244 3.2. Case b: MESSENGER comparison

245 We select a MESSENGER orbit that allows a simulation setup as close  
246 as possible to our theoretical northward IMF case. Due to its mid-day to  
247 midnight orientation (X-Z plane), orbit 1415 (November 8, 2012) provides a



Table 2: Summary of the common input physical and plasma parameters. *SW* denote the solar wind.

	Case (a) Northward IMF	Case (b) MESSENGER
Planetary radius $R_M$ [km]		2440
Planetary dipole moment [nT $\times R_M^3$ ]		200
Northward dipole offset [km]		480
SW proton density [cm $^{-3}$ ]	30	40
SW proton + electron temperature [eV]	21.5+21.5	12+18
SW total plasma $\beta$	1.3	0.69
SW Alfvén Mach number	5	5
SW plasma velocity [km s $^{-1}$ ]	400	459
SW Magnetosonic Mach number	3.5	8.5
IMF (X,Y,Z) components [nT]	(0, 0, +20)	(25, -6, 4.9)
IMF magnitude [nT]	20	26.6

248 close comparison. The orbit has a Disturbance Index of less than 25 [58],  
 249 the lowest magnetic activity quartile, the Z-components of the IMF at the  
 250 inbound an outbound bow shock crossings are positive and within 2 nT of  
 251 each other, and the IMF variability along the entire orbit is less than 10 nT.  
 252 Combining these parameter values indicate stable solar wind conditions.

253

254 We use the inbound part of the orbit to compute the average IMF vector  
 255 to be inserted in our models. Further, the Alfvén Mach number is set to 5, the  
 256 solar wind speed equals 459 km s $^{-1}$  and the proton and electron temperature  
 257 measure 12 eV, and 18 eV, respectively [56, 59].

## 258 4. Results

### 259 4.1. Case a: Northward IMF

260 A purely northward IMF configuration provides a stable magnetosphere  
 261 configuration. We let each model run for 5 minutes, that is, 5 Dungey cycles,  
 262 to reach their respective quasi-stationary states.. Figure 1 shows the solar  
 263 wind proton density maps in the  $X - Z$  (top) and  $X - Y$  (bottom) plane on  
 264 a logarithmic scale, including also velocity lines. The two left panels are the  
 265 results from the MHD codes while the two right panels present the results  
 266 from the hybrid codes. All models have converged to a very similar global  
 267 structure for the Hermean magnetosphere and the characteristic features are  
 268 present: the shape of bowshock, the higher density magnetosheath, and the  
 269 magnetospheric cusps. However, the models do not agree on the proton den-  
 270 sity near the planet and inside the nightside magnetosphere. We also observe  
 271 different locations of the magnetopause structure.

272

273 The  $X - Z$  cut of AMRVAC (Figure 1, upper left-most panel) shows a less  
 274 sharp shock structure at the bow shock, a low density dayside magnetosphere,  
 275 patches of higher density close to the surface in the cusp (which is defined by  
 276 the magnetic field topology) and tail regions, and an asymmetric structure  
 277 for the nightside magnetosphere. The latter is uniquely present in AMRVAC.  
 278 The model also has the largest magnetopause flaring angle among the four  
 279 models. The  $X - Y$  cut of AMRVAC (bottom left-most panel) shows the  
 280 symmetric structure in the dawn-dusk plane. Yagi's MHD code in the  $X - Z$   
 281 plane (upper middle-left panel) presents a sharper bow shock as compared to  
 282 AMRVAC, most likely due to the model's less diffusive scheme. In addition,

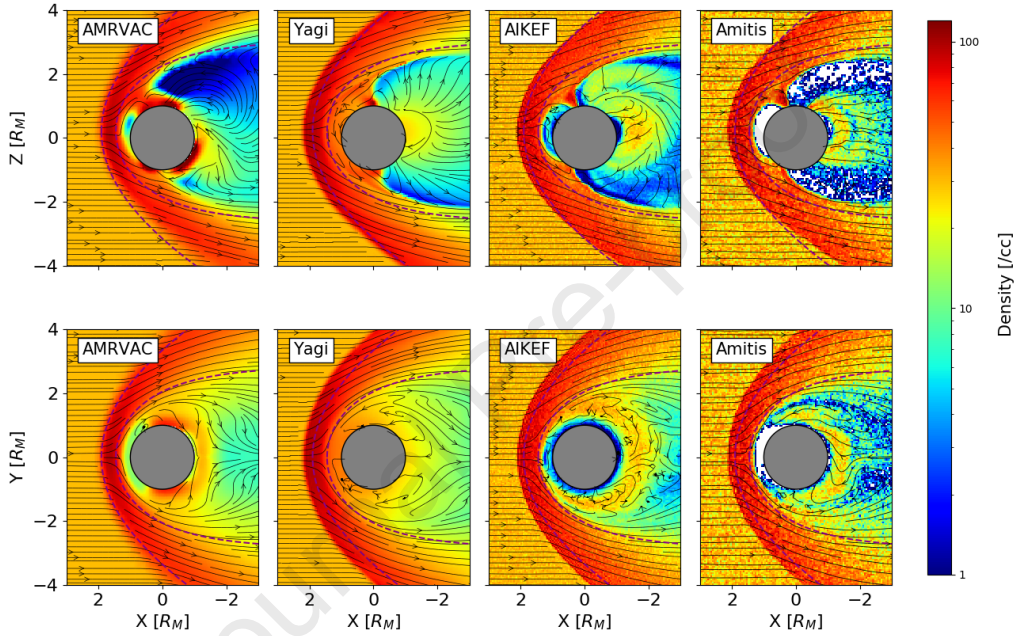


Figure 1: Maps of the solar wind proton density in the X-Z (top) and X-Y (bottom) plane at steady-state for the four simulation models under the northward IMF. The two panels on the left (right) are the results from the MHD (hybrid) codes. Length scales are normalized to the Mercury radius. Black arrows show the bulk velocity stream line and dashed two curves represent the averaged location of bowshock and magnetopause obtained by MESSENGER. [9]

283 the dayside magnetosphere is not dilute and houses a similar density as the  
284 magnetosheath. The nightside structure is more symmetric and slightly tilted  
285 northward. The density concentration we find near the tail region in the  
286 AMRVAC model is not present here. The  $X - Y$  cut of Yagi's model (bottom  
287 middle-left panel) also shows symmetric structure. Compared to AMRVAC,  
288 AMRVAC shows more detailed structure than that of Yagi's. Finally, only  
289 Yagi's model results show a north-south symmetric cusp region. The  $X -$   
290  $Z$  cut of AIKEF (upper middle-right panel), similar to Yagi and Amitis,  
291 produces a sharp bowshock and a more dilute dayside magnetosphere region.  
292 Both hybrid codes concur on narrower cusps as compared to the MHD models  
293 which visually identified. The structure in the nightside is tilted slightly  
294 northward, similar to Yagi's model. AIKEF in the  $X - Y$  plane (bottom  
295 middle-right panel) show small asymmetric structure in the density, e.g.,  
296 higher density inside the magnetosphere in the dawnside while lower density  
297 appears in the duskside.

298 Amitis does not employ any smoothing routines. Operating with a lower  
299 number of particles per cell as compared to AIKEF, the density maps in the  
300  $X - Z$  plane (upper right-most panel) therefore seem to contain more numer-  
301 ical noise. However, the bowshock and magnetopause are clearly captured  
302 and the solar wind plasma is denied from penetrating through the dayside  
303 magnetosphere as in the other simulations. The narrow cusp structure is  
304 similar to the results from AIKEF. The density configuration at the night-  
305 side of the planet seems to tend to northward. On the contrary to AIKEF,  
306 the  $X - Y$  cut (bottom right-most panel) shows the opposite trend, e.g., the  
307 dayside magnetosphere seems to tend to dawnward while in the nightside

308 there is denser plasma close to the surface.

309

310 In order to quantify the differences between the four models, Figure 2  
 311 presents the pressure profile along the subsolar line (X-axis). The dynamic  
 312 and magnetic pressure are extracted and the locations of the bowshock and  
 313 magnetopause have been identified. The four panels correspond to the four  
 314 simulations. The solid lines show the dynamic (ram) pressure,  $\rho \mathbf{v}^2$  where  $\rho$   
 315 and  $\mathbf{v}$  indicate the plasma density and the bulk velocity of the upstream solar  
 316 wind, while the dashed lines represents the magnetic pressure,  $B^2/2\mu_0$  where  
 317  $B$  and  $\mu_0$  denote the magnetic field magnitude and the vacuum permeability,  
 318 respectively. The gray dash-dotted line is the magnetic pressure produced  
 319 by an uncompressed dipole magnetic field with the same dipole moment as  
 320 the models, providing information on how much the planetary magnetic field  
 321 is compressed by the solar wind in each simulation run. The gray vertical  
 322 line at  $x = 1.12 R_M$  indicates the point where the dynamic pressure equals  
 323 the uncompressed magnetic pressure and serves as a reference for the mag-  
 324 netopause location. For each model, the position of the bow shock (BS) has  
 325 been identified as the maximum current density (red vertical solid line). The  
 326 location of the magnetopause (MP; red vertical dashed line) has been identi-  
 327 fied in three different ways: (1) using the position of the most distant closed  
 328 planetary field line that crosses the X-axis, (2) using the position where the  
 329 gas and magnetic pressure are equal, and (3) using the position where the  
 330 current density has its maximum. All three methods were in excellent agree-  
 331 ment for all four models (Table 3).

332

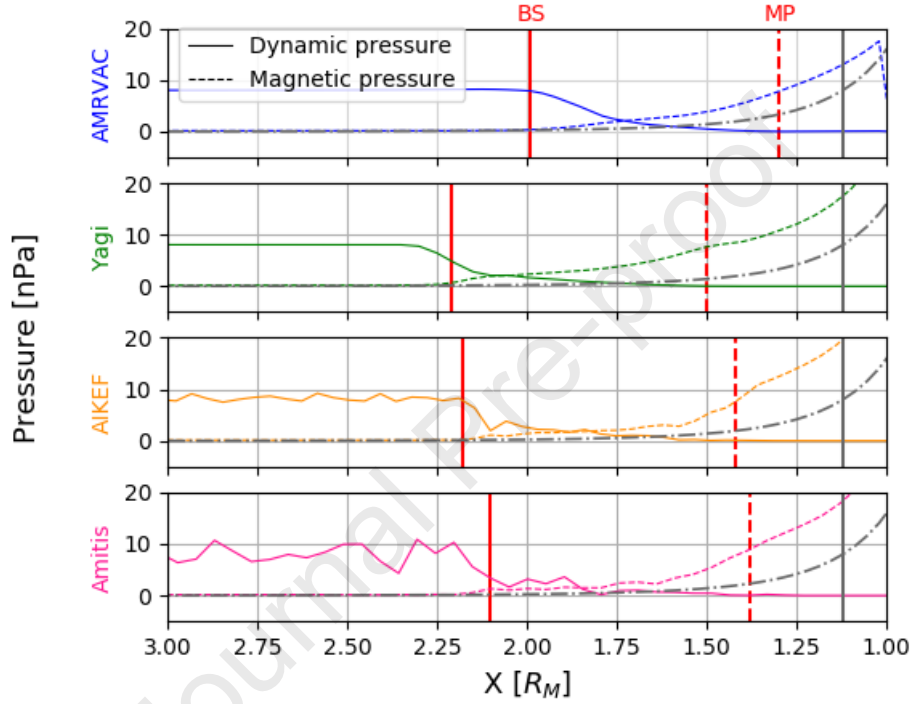


Figure 2: Dynamic (ram) and magnetic pressure profiles along the X-axis (Sun-Mercury direction) from  $3 R_M$  upstream to the planet surface on the dayside for the four simulation codes. The results from the two MHD codes are shown on the top two panels and the hybrid model results on the two bottom panels. The gray dash-dotted line is the magnetic pressure produced by an uncompressed dipole magnetic field with the same dipole moment as the models. The positions of the bow shock (BS) and magnetopause (MP) are shown with red vertical solid and dashed lines. The grey vertical line gives the theoretical expected position of the magnetopause in the case of a radially diminishing magnetic field.

Table 3: Bow shock and magnetopause locations at the subsolar point, and the thickness of the magnetosheath for the four simulation models.

		BS [ $R_M$ ]	MP [ $R_M$ ]	Sheath thickness [ $R_M$ ]	Grid size in X[ $R_M$ ]
MHD	AMRVAC	1.99	1.30	0.69	0.06
	Yagi	2.21	1.50	0.71	0.05
Hybrid	AIKEF	2.18	1.42	0.76	0.04
	Amitis	2.10	1.38	0.72	0.05
	Mean value	2.12	1.40	0.72	
	Standard Deviation	0.085	0.072	0.026	

333 The locations of both the bow shock and magnetopause vary among the  
 334 models with a range of  $0.23 R_M$  and  $0.2 R_M$ , respectively (Figure 2 and Ta-  
 335 ble 3). The mean position of the bow shock and magnetopause is found at  
 336  $2.12 R_M$ , and  $1.40 R_M$ , with a standard deviation of  $\sigma = 0.085$  and  $\sigma = 0.072$ .  
 337 The variation of the magnetopause location is greater than that of the bow  
 338 shock as the former is more sensitive to the boundary condition applied at  
 339 the surface and inside the planet. In an effort to eliminate the effects of the  
 340 numerical implementation for comparison purposes, we compute the average  
 341 thickness of the magnetosheath and find  $0.72 R_M$  with a standard deviation of  
 342  $0.026$ . Thus, differences among models are small and within the uncertainty  
 343 defined by the grid resolution. Note that the mean BS and MP locations  
 344 simulated here with a purely northward IMF are within the ranges measured  
 345 by MESSENGER [9].

346

347 In addition to the bow shock and magnetopause locations along the sub-  
 348 solar line, we further characterize the Hermean magnetosphere by means of

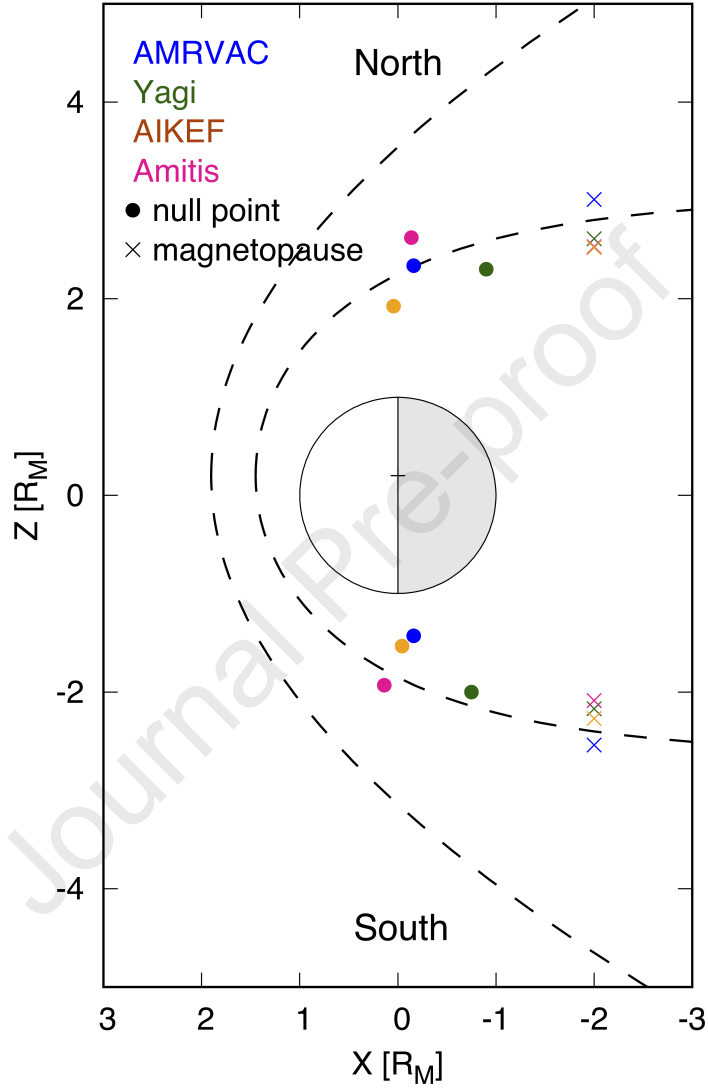


Figure 3: The locations of null points (colored circles) and magnetopause (colored crosses) in the X-Z plane. The dashed lines show the bow shock and magnetopause models defined by Slavin et al. [60] and Shue et al. [61], respectively. The magnetopause paraboloid has parameters  $R_{ss} = 1.45 R_M$  and  $\alpha = 0.5$ . The bow shock model parameters are  $p = 2.75 R_M$ ,  $\epsilon = 1.04$ , and  $X_0 = 0.5 R_M$ .



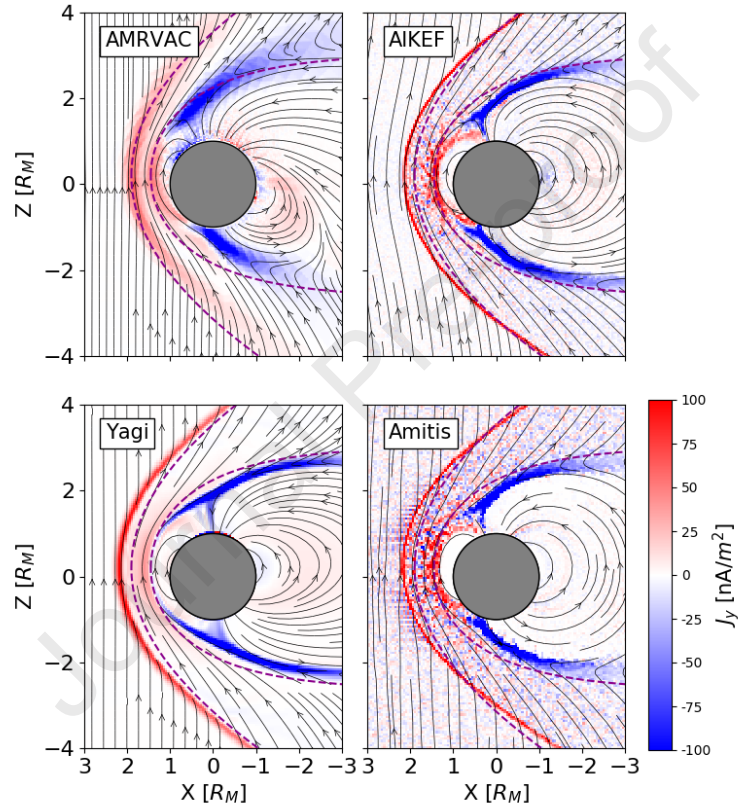


Figure 4: The y component of the current density in  $X - Z$  plane. Black lines with arrow represent the magnetic field line and dashed purple lines are the empirical models of bowshock and magnetopause.

349 the reconnection sites. Figure 3 shows a map in the  $X - Z$  plane with its  
 350 origin at the center of the planet. For reference, the two gray dashed lines  
 351 represent the bow shock and magnetopause locations as predicted by the  
 352 models of Slavin et al. [60], Shue et al. [61], Winslow et al. [9]. The positions  
 353 of the reconnection sites, i.e. the null points, identified from the simulated  
 354 magnetic field structure by our four models are indicated with full colored  
 355 circles. The locations of the magnetopause at  $X = -2 R_M$  are represented  
 356 with colored crosses. On average, the null points near the northern cusp are  
 357 located more towards the nightside, whereas the null point near the south-  
 358 ern cusp are clustered more towards the terminator plane (with exception of  
 359 Yagi's model). Due to the dipole offset towards the north, the southern null  
 360 points are closest to the planet. Note that apart from the chosen plasma field  
 361 conditions also various code-specific parameters, such as numerical resistivity,  
 362 may play a role in where the reconnection sites develop. AMRVAC shows the  
 363 largest north-south asymmetry on the location of null points, which is consis-  
 364 tent with the tilted magnetic structure seen in Figure 1. The locations of the  
 365 magnetopause on the nightside of the planet are obtained from the gradients  
 366 of the density and the current density. With the exception of AMRVAC,  
 367 these are located within the reference magnetopause model ( $R_{ss} = 1.45 R_M$   
 368 and  $\alpha = 0.5$  where  $R_{ss}$  is the magnetopause distance at the subsolar and  $\alpha$   
 369 is the flaring parameter [61, 9]). Given the purely northward IMF, all four  
 370 simulations can be considered in good agreement with the reference models.

371

372 Lastly in this section, the y-component of the current density in  $X -$   
 373  $Z$  plane is presented in Figure 4. Since the IMF is purely northward in

374 this case, we have highlighted only the  $y$ -component of the current density.  
375 Overall, 4 models show similar appearances, i.e., the current enhancement at  
376 the bowshock, positive current at the dayside magnetopause while negative  
377 current generated along the magnetopause in other region. AMRVAC shows  
378 the thicker layer at the bowshock and magnetopause, which is likely due to  
379 the lower grid resolution and Yagi's less diffusive numerical scheme, however,  
380 on the other hand, shock locations in dayside are in good agreement with  
381 the empirical models. Yagi's code shows sharp current structure than that  
382 of AMRVAC and since the magnetic field structure is more symmetric in the  
383 nightside, the current structure also shows more symmetric feature. Although  
384 both two hybrid codes show more busy figure because they treat ions as  
385 the particles, it is difficult to see the peak at the dayside magnetopause.  
386 Compared to Figure 1, since the density inside the dayside magnetosphere  
387 in AIKEF is low, those ions do not affect to the current system.

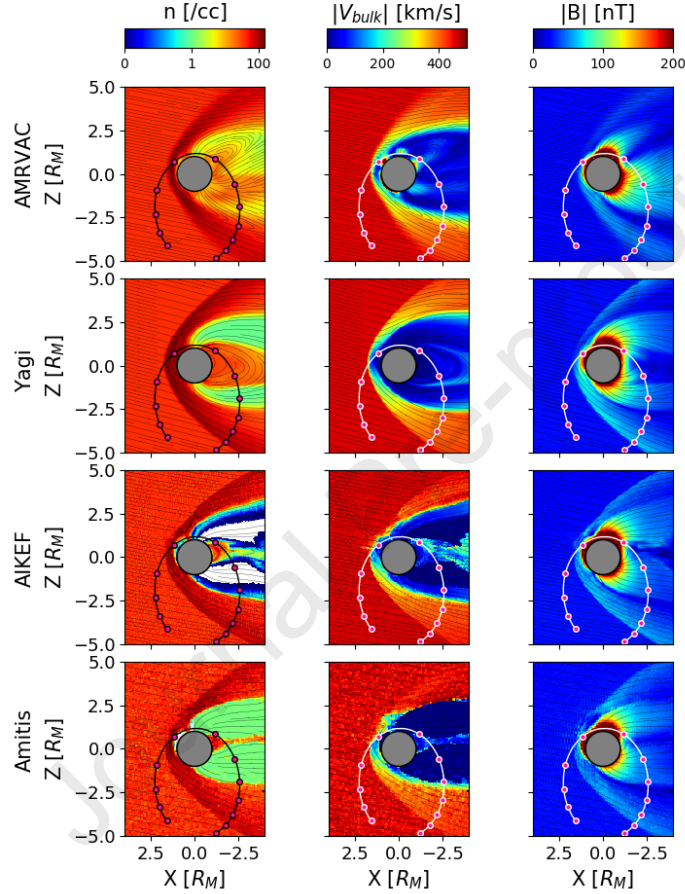


Figure 5: The overview of case  $b$ , from left to right, the panel shows the plasma density, bulk velocity, and magnitude of the magnetic field in  $X - Z$  plane with magnetic field lines. MESSENGER trajectory is marked every 30 min. In this orbit, MESSENGER was first crossing the boundaries in the southern hemisphere, moving into the nightside magnetosphere.

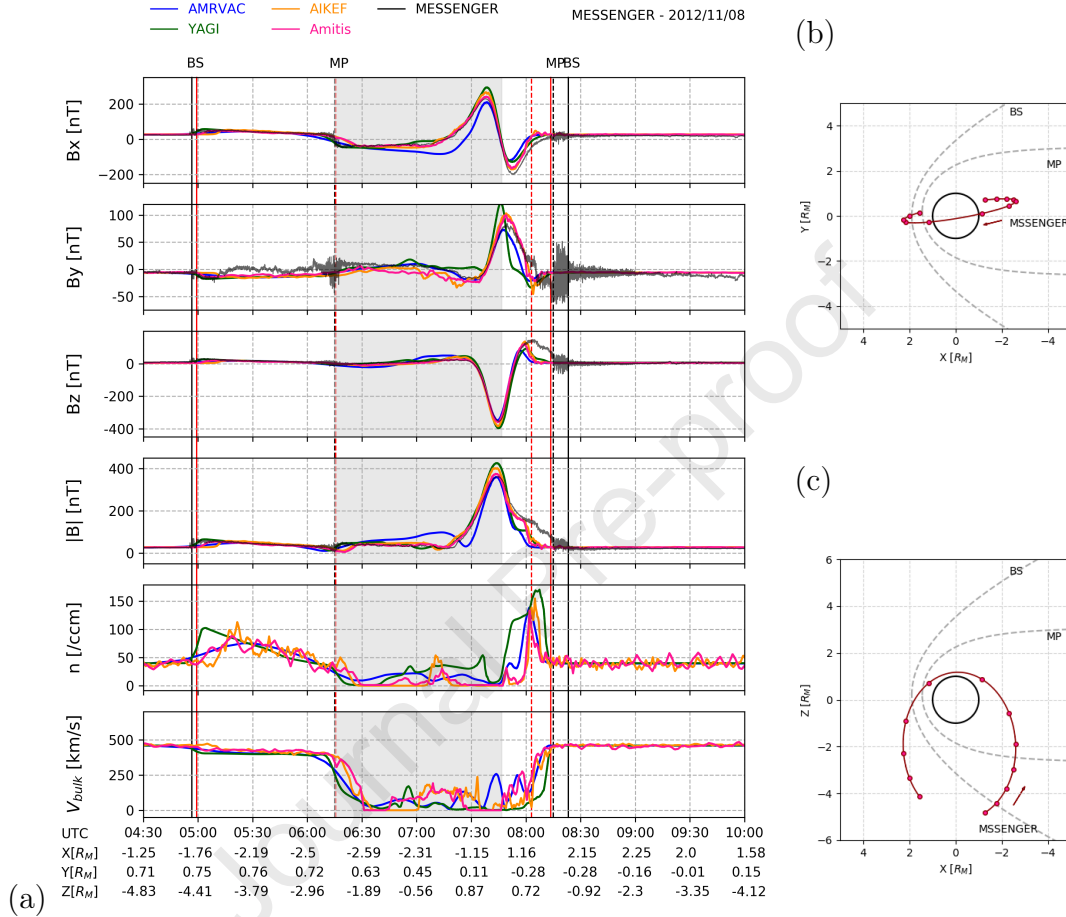


Figure 6: (a) Modeled and observed magnetic field and modeled particle data along orbit 1415 of MESSENGER. Blue, green, orange, and red lines shows the results from AMRVAC, Yagi, AIKEF and Amitis, respectively. The black lines shows the magnetometer data measured by MESSENGER. The bow shock (BS) and magnetopause (MP) crossings identified from the observations are indicated using a vertical solid and dashed black line. The averaged simulated shock and magnetopause crossings are shown by red solid and dashed lines, respectively. The nightside magnetosphere is indicated by a gray background. (b) and (c): the trajectory of MESSENGER spacecraft in  $X - Y$  and  $X - Z$  plane, respectively and the dots indicate 30 minute intervals of the MESSENGER trajectory.

388 *4.2. Case b: MESSENGER comparison*

389 Figure 5 presents overview of the plasma density, the bulk velocity, and  
 390 the magnetic field in  $X - Z$  plane with the MESSENGER trajectory. All  
 391 model results indicate similar features and magnitudes especially in the day-  
 392 side magnetosphere. Interestingly, two hybrid models show the perturbed  
 393 northern magnetopause. Figure 6 presents the magnetic field, density and  
 394 plasma velocity profile along MESSENGER orbit 1415, on 8th of November,  
 395 2012, from 4:30 UT to 10:00 UT (see also section 3.2). The spacecraft en-  
 396 tered the magnetosphere at the nightside along a south- to north-trajectory,  
 397 roughly in the meridian plane with its closest approach near the magnetic  
 398 north of Mercury, thus crossing the bow shock and magnetopause twice. Four  
 399 vertical black lines indicate the bow shock and magnetopause locations for  
 400 both the inbound and outbound crossings observed by MESSENGER. Su-  
 401 perimposed on their respective panels are the simulated profiles from Case *a*  
 402 along the same trajectory. The red vertical lines are the averaged simulated  
 403 shock crossings from the four models. Overall, our models are in close agree-  
 404 ment with the MESSENGER data for the inbound part of the orbit. With  
 405 time differences of up to 12 min, equal to  $\sim 0.28 R_M$  along the spacecraft tra-  
 406 jectory for the inbound orbit, and 17 min ( $\sim 1.1 R_M$ ) for the outbound orbit,  
 407 the locations of the BS and MP agree less well for the outbound section of  
 408 the MESSENGER orbit. The BS locations match better for the inbound  
 409 part of the orbit.

410

411 The variations of the magnetic field along the trajectory seem to be in  
 412 good agreement among codes and with MESSENGER data, while more per-

413 turbed variations in density and bulk velocity profiles. The small fluctuations  
414 in two hybrid are results of particle noises.

415 Since we used the inbound part of the orbit to constrain the upstream  
416 plasma parameters to initialize the simulations, it is possible that variations  
417 in the solar wind dynamic pressure during the orbit may be responsible for  
418 the larger discrepancy in the outbound part of the orbit. Interestingly, there  
419 are distinct differences between the MHD and the hybrid codes (panel 4 of  
420 Figure 6). Around 7:50 UT, when the spacecraft is inside the dayside magne-  
421 tosheath, the results from the two hybrid simulations are in agreement with  
422 the observations, while both MHD models predict a lower magnetic field in-  
423 tensity. The spacecraft passes through the northern cusp and then moves  
424 towards the dayside region. At 8:10 UT, near the peak density, we find the  
425 compressed magnetosheath plasma. As expected, also the density and veloc-  
426 ity profiles predicted by the hybrid codes show steeper profiles at the shock  
427 crossing compared to the MHD models.

428

## 429 5. Discussion

### 430 5.1. Case b: MESSENGER comparison

431 Due to the limited particle instrumentation on board the single-spacecraft  
432 MESSENGER mission, it is not possible to constrain the exact solar wind  
433 plasma parameters to set up a comparison simulation. More precisely, be-  
434 cause the particle instrument onboard MESSENGER was protected by the  
435 sun shield and thus it had a limited field of view, this condition prevented the  
436 instrument from observing the majority of solar wind. Therefore, density and

437 velocity, temperature of solar wind cannot be derived and those parameters  
438 must be assumed when input parameters were considered [62] In addition,  
439 the solar wind varies in time and may even be changing significantly while  
440 MESSENGER crosses the magnetosphere. This may be the reason for some  
441 of the discrepancies between simulated and measured profiles. In Figure 7  
442 we compute the difference between the observed and modeled magnetic fields  
443 along our chosen MESSENGER orbit. We exclude the time frame between  
444 the two MP crossings (from 6:15 UT to 7:45 UT) while MESSENGER passed  
445 the nightside region of the magnetosphere (indicated by a gray background),  
446 to focus on the cusp and boundary layer locations.

447

448 Just before 5:00 UT, MESSENGER crosses the BS for the first time,  
449 about 3 min before the predicted averaged time stamp from our models. Con-  
450 tinuing along the trajectory, both the modeled X- and Z-component agree  
451 well with MESSENGER, whereas the models underestimate the magnetic  
452 field contribution by roughly 15 nT along the Y direction. Our models agree  
453 on the inbound MP crossing time at 6:15 UT within a 5 min time range. At  
454 7:50 UT, when MESSENGER moves from the nightside to the dayside in the  
455 northern hemisphere, all four models predict a magnetic pile-up, although  
456 none of the models fully reproduces the fine-scale structure. Immediately  
457 following the pile-up, the models underestimate the magnetic field strength  
458 by roughly 100 nT. Note that the different profiles in Figure 6 show no real  
459 ‘winner’ among the four simulation models as all codes show different small-  
460 scale discrepancies with the MESSENGER measurements at the boundaries  
461 between the distinct plasma regions of Mercury’s magnetosphere. It shows



462 the need for a multi-spacecraft mission, such as BepiColombo, to simulta-  
463 neously measure the local Hermean and upstream plasma environment in  
464 order to fine-tune the inputs to numerical models and in turn characterize  
465 Mercury’s global plasma environment.

466

### 467 *5.2. Virtual sampling along Mio/MPO orbits*

468 One of the major goals of the SHOTS project, next to comparing differ-  
469 ent simulation approaches with available MESSENGER measurements, is to  
470 help prepare the community for the forthcoming BepiColombo mission by  
471 making available a catalog of simulation that showcases the plasma struc-  
472 ture and dynamics of Mercury’s magnetosphere under different solar wind  
473 conditions. In the first step of this project, we chose four different (MHD  
474 and hybrid) simulation models. Figures 8 and 9 show the plasma character-  
475 istics expected along a typical Mio and MPO orbit, respectively, during the  
476 planned nominal orbital phase of BepiColombo. We chose the upstream solar  
477 wind conditions identical to the MESSENGER case studied above (Case *b*  
478 in Table 2). For ease of comparison, the orbital plane is set perpendicular  
479 to the X direction, corresponding to BepiColombo’s operations planned for  
480 April 4, 2026. During this period, both Mio and MPO remain inside the  
481 magnetosphere and the plasma environment will be fully observed by the  
482 magnetometers on board Mio and MPO [63, 64], the Mercury Plasma Parti-  
483 cle Experiment (MPPE) [65] and the Plasma Wave Investigation (PWI) [66]  
484 onboard Mio, and the Search for Exospheric Refilling and Emitted Natural  
485 Abundances (SERENA) on board MPO [67].

486

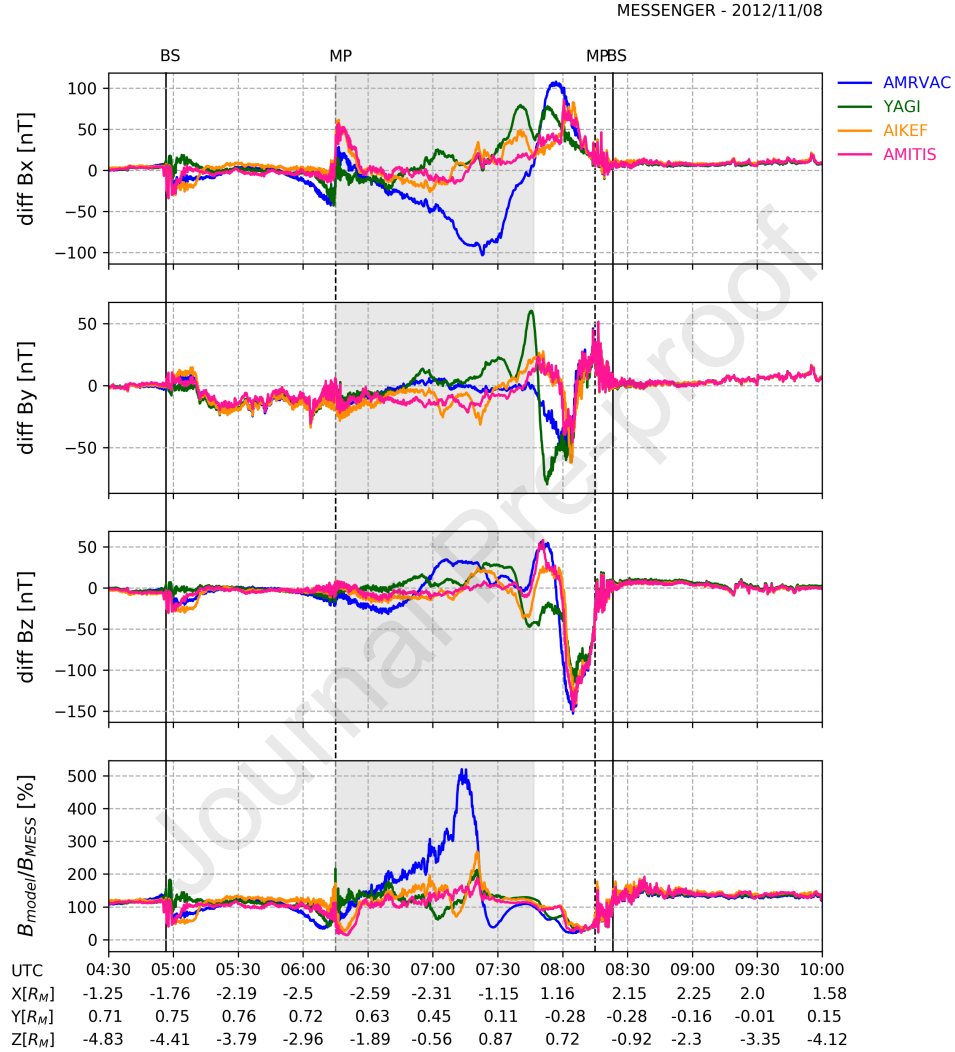


Figure 7: Difference between the simulation results and the MESSENGER magnetic field measurements ( $B_{model} - B_{MESS}$ ). The bow shock (BS) and magnetopause (MP) crossings identified from the observations are indicated with a vertical solid and dashed line, respectively and the region MESSENGER passing through inside the nightside magnetosphere is indicated by a gray background.

487 In both Figures 8 and 9 the solid vertical lines indicate the southern  
488 ( $T_S$ ) and northern ( $T_N$ ) terminator crossing and the dashed vertical line is  
489 the time when the spacecraft crosses the sub-solar point (SSP). During this  
490 period, Mio will be moving along the frontside magnetopause (from 15:15  
491 UT to 15:35 UT) where our models predict an enhancement of the magnetic  
492 field intensity and plasma velocity. Note that the predicted profiles closest to  
493 the planet are not in agreement, possibly due to the numerical treatment of  
494 the planetary boundary condition (see also Figure 1). Next, Mio will move  
495 across the cusp region and re-enter the nightside magnetosphere from the  
496 north. Large discrepancies among models around the subsolar point to the  
497 northern terminator can be explained by the orbit of the Mio spacecraft.  
498 Since Mio is moving along the magnetopause, different locations of the mag-  
499 netopause in each model are critical. Mio is clearly inside the magnetopause  
500 in AIKEF and Amitis around the subsolar point but probably not in Yagi  
501 and AMRVAC. After crossing subsolar point around 15:17 UT, the density  
502 and velocity profiles diverge. A similar trend is not visible in the magnetic  
503 field predictions. This may be the region where the ion dynamics has the  
504 largest impact, i.e., the finite Larmor radius effect of particle must be taken  
505 into account in the magnetosheath, hence producing the largest differences  
506 between the hybrid and MHD models.

507

508 MPO will orbit significantly closer to the planet. The spacecraft will leave  
509 the southern magnetosphere via the nightside, then crosses the terminator  
510 and enters the dayside magnetosphere. Just before 15:00 UT and around  
511 15:35 UT, the two hybrid models and AMRVAC predict a significant density

512 enhancement, indicating the presence of trapped particles while Yagi show  
513 significantly different appearance. In Yagi's model, the dayside magneto-  
514 sphere is not clearly seen (see Figure 5), and thus, the spacecraft seems to  
515 observe rather the magnetosheath component than the component inside the  
516 magnetopause at the time between 14:30 UT to 14:50 UT. The spacecraft  
517 passes through the cusp region (light blue areas in Figure 9). MPO's tra-  
518 jectory will be most useful to better understand the structure and dynamics  
519 of the magnetosphere closest to the planet and in particular near the south-  
520 ern hemisphere. This region has been explored less due to MESSENGER's  
521 highly inclined and eccentric orbit.

522

523 Sampling the virtual orbits of Mio and MPO for a variety of solar wind  
524 parameters and/or models, we will be able to predict when the spacecraft  
525 most likely cross the cusp, the plasma sheet and the shocked regions within  
526 certain margins. These margins depend on the characteristics of the sim-  
527 ulation and the physical processes included in the model. The combined  
528 measurements from the two spacecraft will provide a wealth of information  
529 on the Hermean plasma environment, however, to reproduce adequately the  
530 environment in 3D, numerical 3D models are essential. Thus, making predic-  
531 tive simulations with the information by combined spacecraft measurements  
532 a necessity to maximize the scientific return of the mission. To this effect, the  
533 simulation domain needs to be extended farther downstream of the planet  
534 to capture better the magnetotail region. Also temporal information needs  
535 to be included. In this study, our hybrid models have not implemented its  
536 tenuous exosphere based on the previous works [23, 33] that shows Mercury's

537 exosphere is tenuous enough to not significantly affect on Mercury's magne-  
538 topheric system. Our first goal was to purely compare between MHD and  
539 hybrid simulations so that we see the ion kinetics. However revealing the role  
540 of the exosphere is also the one of the key questions of Mercury's science. It  
541 will be investigated further in near future. Finally, also Particle-In-Cell and  
542 Vlasov simulations that include the electron dynamics are needed.

543

## 544 **6. Conclusions**

545 We have compared the results of four different (MHD and hybrid) global  
546 simulation models with the same input parameters to simulate the solar wind  
547 interaction with Mercury's dayside magnetosphere. Because the effect of the  
548 existence of its tenuous exosphere is small to affect the structure of Mercury's  
549 magnetosphere, the exosphere has not been implemented in our models. All  
550 our models produced a similar global structure in the dayside consistent with  
551 empirical (analytical) fits for the locations of the bow shock and the mag-  
552 netopause. In contrast to the dayside magnetosphere, although it is out of  
553 our scope, the magnetic field configuration in the nightside magnetosphere  
554 differs among models, and the plasma distribution and bulk velocity close  
555 to the surface are also different. The significant difference between MHD  
556 and hybrid models is not seen in this study, thus, the differences between  
557 the simulations predictions seem to be caused numerically, i.e., the planetary  
558 boundary conditions, different size of the grid, numerical scheme, rather than  
559 the self-consistent ion kinetics included in the model.

560

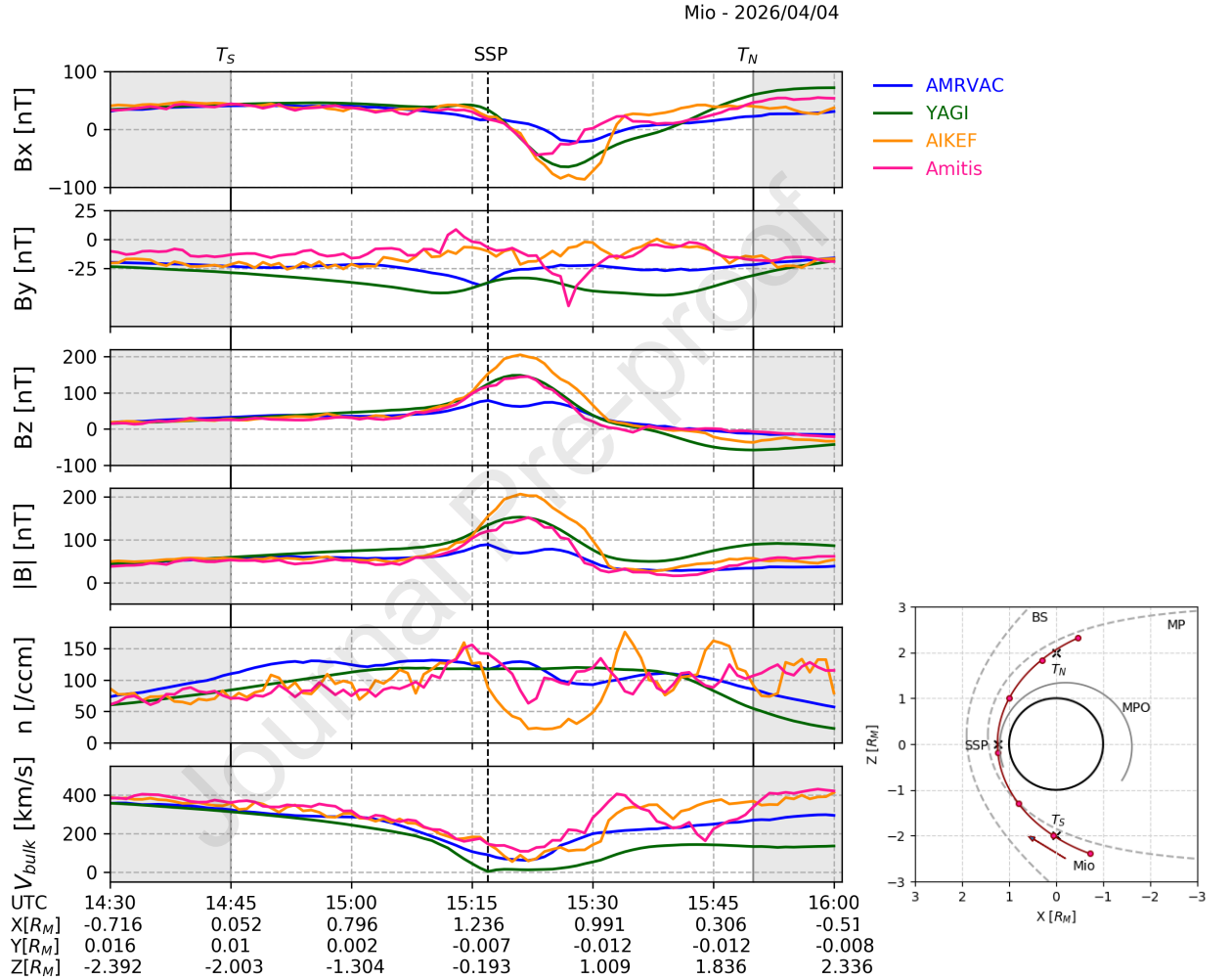


Figure 8: Magnetic field and particle data along a representative Mio orbit. The red dots along the trajectory in the inset panel show the position of the spacecraft along 15 min intervals. The solid vertical lines indicate the crossing of the southern ( $T_S$ ) and northern ( $T_N$ ) terminator, the dashed vertical line is the time when the spacecraft crosses the subsolar point (SSP). The nightside region ( $X < 0$ ) is indicated by a gray background.

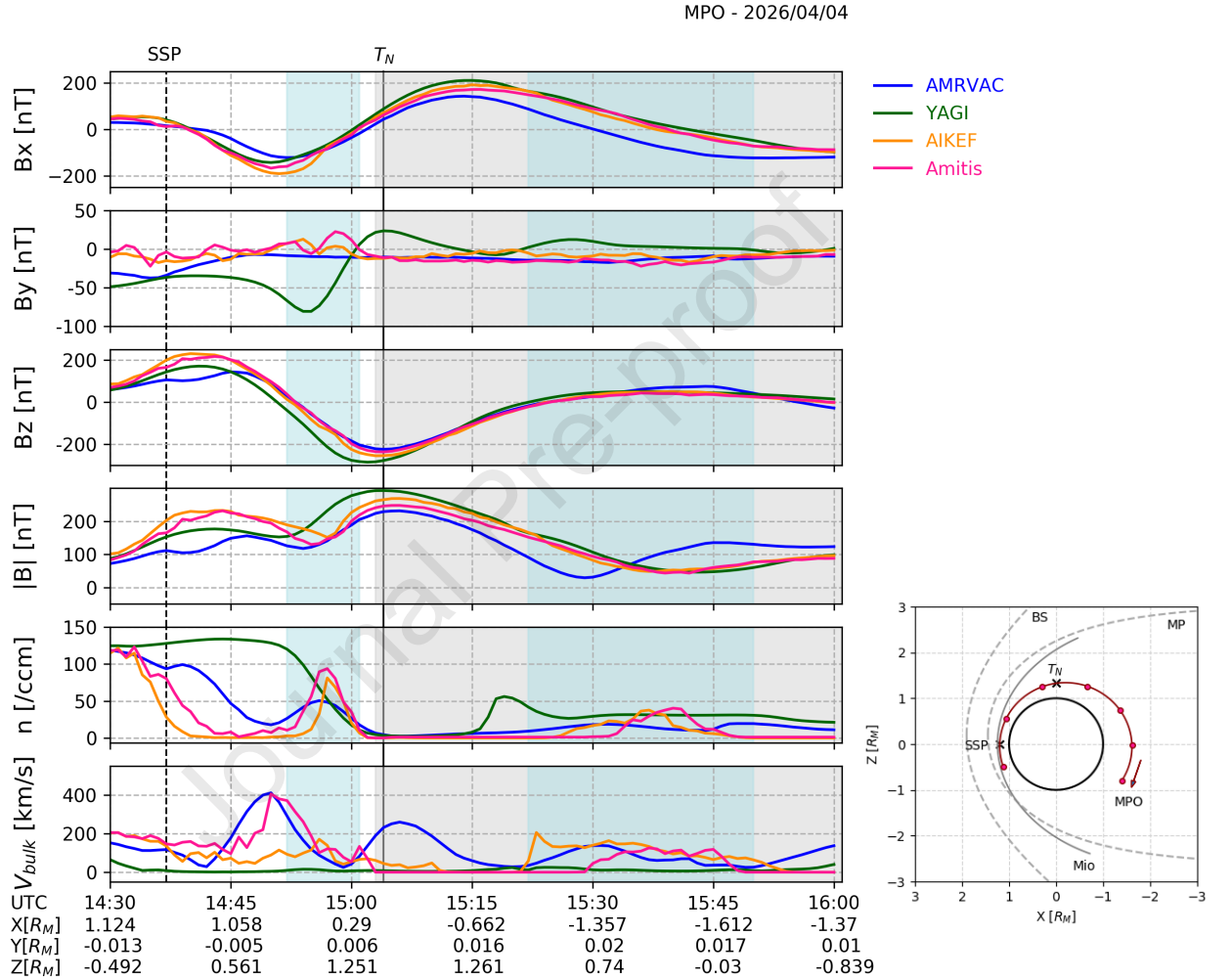


Figure 9: Magnetic field and particle data along a representative MPO orbit. The red dots along the trajectory in the inset panel show the position of the spacecraft along 15 min intervals. The solid vertical lines indicate northern ( $T_N$ ) terminator and the dashed vertical line is the time when the spacecraft crosses the subsolar point (SSP). The nightside region ( $X < 0$ ) is indicated by a gray background.

561 We cross-compared our results with a theoretical northward IMF scenario  
562 (Case *a*) and MESSENGER orbit 1415 (Case *b*), indicated to have stable so-  
563 lar wind conditions with a northward IMF similar to the theoretical case. In  
564 Case *a*, the standard deviations for the predicted mean locations of the bow  
565 shock, magnetopause and the thickness of magnetosheath are small. For Case  
566 *b*, during the inbound part of the orbit, time differences for the bow shock  
567 and the magnetopause crossings are found up to 12 minutes, corresponding  
568 to a distance along the orbit of  $0.28 R_M$ . For the outbound section of the  
569 orbit, the maximum time difference increased to 17 minutes, equivalent to  
570  $1.1 R_M$ .

571

572 One of the major goals of SHOTS is to prepare a catalog of simulations  
573 that can predict the plasma environment in- and outside the Hermean mag-  
574 netosphere under different solar wind conditions, in this way contributing to  
575 maximizing the scientific return of the forthcoming BepiColombo observa-  
576 tions. Here, for the first time, we have extracted the data from our mod-  
577 els along representative Mio and MPO orbits. A long-lasting project-based  
578 and community-wide effort will be important both for the forthcoming Bepi-  
579 Colombo's Mercury flybys and during its nominal orbital phase.

580

## 581 Acknowledgments

582 The authors acknowledge support from the French space plasma physics  
583 data centre (Centre de Données de la Physique des Plasmas, CDPP: [http://](http://www.cdpp.eu)  
584 [www.cdpp.eu](http://www.cdpp.eu) funded by CNES and CNRS). J.D. acknowledges support from



585 NASA's Solar System Exploration Research Virtual Institute (SSERVI): In-  
586 stitute for Modeling Plasmas, Atmosphere, and Cosmic Dust (IMPACT),  
587 and the NASA High-End Computing (HEC) Program through the NASA  
588 Advanced Supercomputing (NAS) Division at Ames Research Center. D.H.  
589 was supported by the German Ministerium für Wirtschaft und Energie and  
590 the German Zentrum für Luft-und Raumfahrt under contract 50 QW 1501.  
591 W.E. was supported by DFG (German Research Foundation) under con-  
592 tract HE8016/1-1. S.F. acknowledges support from Swedish National Re-  
593 search Council, grant #2018- 03454, Swedish National Space Agency, grants  
594 #2018-C and #2018-N. Amitis simulations conducted using computational  
595 resources provided by the Swedish National Infrastructure for Computing  
596 (SNIC), projects SNIC2019/3-178 and SNIC2020-5-101 at the High Per-  
597 formance Computing Center North (HPC2N), Umeå University, Sweden.  
598 French co-authors would like to acknowledge the support of CNES for the  
599 BepiColombo mission. Part of this work has been done in the framework of  
600 the Sun Planet Interactions Digital Environment on Request (SPIDER) ac-  
601 tivities of the Europlanet 2024 RI project. Europlanet 2024 RI has received  
602 funding from the European Union's Horizon 2020 research and innovation  
603 programme under grant agreement No 871149.

604

605 All data necessary to validate the findings presented in this manuscript  
606 can be found at [https://github.com/jandeca/Aizawa\\_etal\\_PSS\\_2020](https://github.com/jandeca/Aizawa_etal_PSS_2020) (DOI:  
607 to be provided) in accordance with the Findability Accessibility, Interoper-  
608 ability, and Reuse (FAIR) principles. The magnetometer data from the MES-  
609 SENDER observations are available in the Planetary Data System (<https://>

610 //pds-ppi.igpp.ucla.edu).

611

612 [1] N. F. Ness, K. W. Behannon, R. P. Lepping, Y. C. Whang, The magnetic  
613 field of Mercury, *Journal of Geophysical Research* (1896-1977) 80 (1975)  
614 2708–2716. doi:10.1029/JA080i019p02708.

615 [2] Y. C. Whang, Magnetospheric magnetic field of Mercury, *Journal of*  
616 *Geophysical Research* (1896-1977) 82 (1977) 1024–1030. doi:10.1029/  
617 JA082i007p01024.

618 [3] H. Korth, B. J. Anderson, C. L. Johnson, J. A. Slavin, J. M. Raines,  
619 T. H. Zurbuchen, Structure and configuration of Mercury’s magneto-  
620 sphere, in: S. C. Solomon, L. R. Nittler, B. J. Anderson (Eds.), *Mercury:*  
621 *The View after MESSENGER*, Cambridge University Press, 2018, pp.  
622 430–460.

623 [4] J. A. Slavin, D. N. Baker, D. J. Gershman, G. C. Ho, S. M. Imber, S. M.  
624 Krimigis, T. Sundberg, Mercury’s dynamic magnetosphere, in: S. C.  
625 Solomon, L. R. Nittler, B. J. Anderson (Eds.), *Mercury: The View after*  
626 *MESSENGER*, Cambridge University Press, 2018, pp. 461–496.

627 [5] E. Jang, J. T. Zhao, C. Yue, Q. G. Zong, Y. Liu, Z. Y. Liu, Energetic  
628 Ion Dynamics Near the Cusp Region of Mercury, *The Astrophysical*  
629 *Journal* 892 (2020) 10. doi:10.3847/1538-4357/ab74d1.

630 [6] J. A. Slavin, M. H. Acuña, B. J. Anderson, D. N. Baker, M. Benna,  
631 G. Gloeckler, R. E. Gold, G. C. Ho, R. M. Killen, H. Korth, S. M.  
632 Krimigis, R. L. McNutt, L. R. Nittler, J. M. Raines, D. Schriver, S. C.

- 633 Solomon, R. D. Starr, P. Trávníček, T. H. Zurbuchen, Mercury's Mag-  
634 netosphere After MESSENGER's First Flyby, *Science* 321 (2008) 85–89.  
635 doi:10.1126/science.1159040.
- 636 [7] J. A. Slavin, M. H. Acuña, B. J. Anderson, D. N. Baker, M. Benna,  
637 S. A. Boardsen, G. Gloeckler, R. E. Gold, G. C. Ho, H. Korth, S. M.  
638 Krimigis, R. L. McNutt, J. M. Raines, M. Sarantos, D. Schriver, S. C.  
639 Solomon, P. Trávníček, T. H. Zurbuchen, Messenger observations of  
640 magnetic reconnection in Mercury's magnetosphere, *Science* 324 (2009)  
641 606–610. doi:10.1126/science.1172011.
- 642 [8] J. A. Slavin, B. J. Anderson, D. N. Baker, M. Benna, S. A. Boardsen,  
643 G. Gloeckler, R. E. Gold, G. C. Ho, H. Korth, S. M. Krimigis, R. L.  
644 McNutt, L. R. Nittler, J. M. Raines, M. Sarantos, D. Schriver, S. C.  
645 Solomon, R. D. Starr, P. M. Trávníček, T. H. Zurbuchen, Messenger  
646 observations of extreme loading and unloading of Mercury's magnetic  
647 tail, *Science* 329 (2010) 665–668. doi:10.1126/science.1188067.
- 648 [9] R. M. Winslow, B. J. Anderson, C. L. Johnson, J. A. Slavin, H. Korth,  
649 M. E. Purucker, D. N. Baker, S. C. Solomon, Mercury's magnetopause  
650 and bow shock from MESSENGER Magnetometer observations, *Journal*  
651 *of Geophysical Research (Space Physics)* 118 (2013) 2213–2227. doi:10.  
652 1002/jgra.50237.
- 653 [10] J. A. Slavin, G. A. DiBraccio, D. J. Gershman, S. M. Imber, G. K. Poh,  
654 J. M. Raines, T. H. Zurbuchen, X. Jia, D. N. Baker, K.-H. Glassmeier,  
655 S. A. Livi, S. A. Boardsen, T. A. Cassidy, M. Sarantos, T. Sundberg,  
656 A. Masters, C. L. Johnson, R. M. Winslow, B. J. Anderson, H. Korth,

- 657 R. L. McNutt Jr., S. C. Solomon, Messenger observations of Mercury's  
658 dayside magnetosphere under extreme solar wind conditions, *Journal*  
659 *of Geophysical Research: Space Physics* 119 (2014) 8087–8116. doi:10.  
660 1002/2014JA020319.
- 661 [11] X. Jia, J. A. Slavin, G. Poh, G. A. DiBraccio, G. Toth, Y. Chen,  
662 J. M. Raines, T. I. Gombosi, Messenger observations and global  
663 simulations of highly compressed magnetosphere events at Mercury,  
664 *Journal of Geophysical Research: Space Physics* 124 (2019) 229–  
665 247. URL: [https://agupubs.onlinelibrary.wiley.com/doi/abs/](https://agupubs.onlinelibrary.wiley.com/doi/abs/10.1029/2018JA026166)  
666 [10.1029/2018JA026166](https://agupubs.onlinelibrary.wiley.com/doi/abs/10.1029/2018JA026166). doi:10.1029/2018JA026166.
- 667 [12] J. A. Slavin, H. R. Middleton, J. M. Raines, X. Jia, J. Zhong, W.-J. Sun,  
668 S. Livi, S. M. Imber, G.-K. Poh, M. Akhavan-Tafti, J. M. Jasinski, G. A.  
669 DiBraccio, C. Dong, R. M. Dewey, M. L. Mays, Messenger observations  
670 of disappearing dayside magnetosphere events at Mercury, *Journal of*  
671 *Geophysical Research: Space Physics* 124 (2019) 6613–6635. doi:10.  
672 1029/2019JA026892.
- 673 [13] R. M. Winslow, N. Lugaz, L. Philpott, C. J. Farrugia, C. L. Johnson,  
674 B. J. Anderson, C. S. Paty, N. A. Schwadron, M. A. Asad, Observations  
675 of Extreme ICME Ram Pressure Compressing Mercury's Dayside Mag-  
676 netosphere to the Surface, *The Astrophysical Journal* 889 (2020) 184.  
677 doi:10.3847/1538-4357/ab6170. arXiv:1903.00577.
- 678 [14] E. Kallio, P. Wurz, R. Killen, S. McKenna-Lawlor, A. Milillo, A. Mura,  
679 S. Massetti, S. Orsini, H. Lammer, P. Janhunen, On the impact of  
680 multiply charged heavy solar wind ions on the surface of Mercury, the

- 681 Moon and Ceres, *Planetary and Space Science* 56 (2008) 1506–1516.  
682 doi:10.1016/j.pss.2008.07.018.
- 683 [15] J. M. Raines, D. J. Gershman, J. A. Slavin, T. H. Zurbuchen, H. Korth,  
684 B. J. Anderson, S. C. Solomon, Structure and dynamics of Mercury's  
685 magnetospheric cusp: MESSENGER measurements of protons  
686 and planetary ions, *Journal of Geophysical Research (Space Physics)*  
687 119 (2014) 6587–6602. doi:10.1002/2014JA020120.
- 688 [16] S. Fatemi, A. R. Poppe, S. Barabash, Hybrid simulations of solar  
689 wind proton precipitation to the surface of Mercury, *Journal  
690 of Geophysical Research: Space Physics* 125 (2020) e2019JA027706.  
691 doi:10.1029/2019JA027706.
- 692 [17] X. Jia, J. A. Slavin, T. I. Gombosi, L. K. S. Daldorff, G. Toth, B. van der  
693 Holst, Global mhd simulations of Mercury's magnetosphere with coupled  
694 planetary interior: Induction effect of the planetary conducting core on  
695 the global interaction, *Journal of Geophysical Research: Space Physics*  
696 120 (2015) 4763–4775. doi:10.1002/2015JA021143.
- 697 [18] C. L. Johnson, L. C. Philpott, B. J. Anderson, H. Korth, S. A. Hauck,  
698 D. Heyner, R. J. Phillips, R. M. Winslow, S. C. Solomon, MESSENGER  
699 observations of induced magnetic fields in Mercury's core, *Geophysical  
700 Research Letters* 43 (2016) 2436–2444. doi:10.1002/2015GL067370.
- 701 [19] K. Kabin, T. Gombosi, D. DeZeeuw, K. Powell, Interaction of Mercury  
702 with the solar wind, *Icarus* 143 (2000) 397 – 406. doi:http://dx.doi.  
703 org/10.1006/icar.1999.6252.

- 704 [20] M. Benna, B. J. Anderson, D. N. Baker, S. A. Boardsen, G. Gloeckler,  
705 R. E. Gold, G. C. Ho, R. M. Killen, H. Korth, S. M. Krimigis, M. E.  
706 Purucker, R. L. McNutt, J. M. Raines, W. E. McClintock, M. Sarantos,  
707 J. A. Slavin, S. C. Solomon, T. H. Zurbuchen, Modeling of the magne-  
708 tosphere of Mercury at the time of the first MESSENGER flyby, *Icarus*  
709 209 (2010) 3–10. doi:10.1016/j.icarus.2009.11.036.
- 710 [21] C. Dong, L. Wang, A. Hakim, A. Bhattacharjee, J. A. Slavin, G. A.  
711 DiBraccio, K. Germaschewski, Global Ten-Moment Multifluid Simu-  
712 lations of the Solar Wind Interaction with Mercury: From the Plan-  
713 etary Conducting Core to the Dynamic Magnetosphere, *Geophysical*  
714 *Research Letters* 46 (2019) 11,584–11,596. doi:10.1029/2019GL083180.  
715 arXiv:1904.02695.
- 716 [22] E. Kallio, P. Janhunen, Modelling the solar wind interaction with Mer-  
717 cury by a quasi-neutral hybrid model, *Annales Geophysicae* 21 (2003)  
718 2133–2145. doi:10.5194/angeo-21-2133-2003.
- 719 [23] E. Kallio, P. Janhunen, The response of the hermean mag-  
720 netosphere to the interplanetary magnetic field, *Advances in*  
721 *Space Research* 33 (2004) 2176 – 2181. URL: [http://www.](http://www.sciencedirect.com/science/article/pii/S0273117703004472)  
722 [sciencedirect.com/science/article/pii/S0273117703004472](http://www.sciencedirect.com/science/article/pii/S0273117703004472).  
723 doi:[https://doi.org/10.1016/S0273-1177\(03\)00447-2](https://doi.org/10.1016/S0273-1177(03)00447-2), mercury,  
724 Mars and Saturn.
- 725 [24] P. Trávníček, P. Hellinger, D. Schriver, Structure of Mercury’s magne-  
726 tosphere for different pressure of the solar wind: Three dimensional

- 727 hybrid simulations, *Geophysical Research Letters* 34 (2007) 5104.  
728 doi:10.1029/2006GL028518.
- 729 [25] P. M. Trávníček, D. Schriver, P. Hellinger, D. Herčík, B. J. An-  
730 derson, M. Sarantos, J. A. Slavin, Mercury's magnetosphere: so-  
731 lar wind interaction for northward and southward interplanetary mag-  
732 netic field: Hybrid simulation results, *Icarus* 209 (2010) 11 – 22.  
733 doi:http://dx.doi.org/10.1016/j.icarus.2010.01.008.
- 734 [26] Y.-C. Wang, J. Mueller, U. Motschmann, W.-H. Ip, A hybrid simulation  
735 of Mercury's magnetosphere for the MESSENGER encounters in year  
736 2008, *Icarus* 209 (2010) 46–52. doi:10.1016/j.icarus.2010.05.020.
- 737 [27] E. Richer, R. Modolo, G. M. Chanteur, S. Hess, F. Leblanc, A global  
738 hybrid model for Mercury's interaction with the solar wind: Case study  
739 of the dipole representation, *Journal of Geophysical Research (Space*  
740 *Physics)* 117 (2012) A10228. doi:10.1029/2012JA017898.
- 741 [28] D. Herčík, P. M. Trávníček, J. R. Johnson, E.-H. Kim, P. Hellinger, Mir-  
742 ror mode structures in the asymmetric hermean magnetosheath: Hybrid  
743 simulations, *Journal of Geophysical Research: Space Physics* 118 (2013)  
744 405–417. doi:10.1029/2012JA018083.
- 745 [29] D. Herčík, P. M. Trávníček, Š. Štverák, P. Hellinger, Properties of her-  
746 mean plasma belt: Numerical simulations and comparison with mes-  
747 senger data, *Journal of Geophysical Research: Space Physics* 121  
748 (2016) 413–431. URL: [https://agupubs.onlinelibrary.wiley.com/](https://agupubs.onlinelibrary.wiley.com/doi/abs/10.1002/2015JA021938)  
749 [doi/abs/10.1002/2015JA021938](https://agupubs.onlinelibrary.wiley.com/doi/abs/10.1002/2015JA021938). doi:10.1002/2015JA021938.

- 750 [30] S. Fatemi, A. R. Poppe, G. T. Delory, W. M. Farrell, Amitis: A 3D  
751 GPU-based hybrid-PIC model for space and plasma physics, *Journal of*  
752 *Physics: Conference Series* 837 (2017) 012017.
- 753 [31] S. Fatemi, N. Poirier, M. Holmström, J. Lindkvist, M. Wieser,  
754 S. Barabash, A modelling approach to infer the solar wind dynamic pres-  
755 sure from magnetic field observations inside Mercury’s magnetosphere,  
756 *Astronomy & Astrophysics* 614 (2018) A132. doi:10.1051/0004-6361/  
757 201832764.
- 758 [32] W. Exner, D. Heyner, L. Liuzzo, U. Motschmann, D. Shiota, K. Kusano,  
759 T. Shibayama, Coronal mass ejection hits Mercury: A.I.K.E.F. hybrid-  
760 code results compared to messenger data, *Planetary and Space Science*  
761 153 (2018) 89 – 99.
- 762 [33] W. Exner, S. Simon, D. Heyner, U. Motschmann, Influence of Mer-  
763 cury’s Exosphere on the Structure of the Magnetosphere, *Journal of*  
764 *Geophysical Research (Space Physics)* 125 (2020) e27691. doi:10.1029/  
765 2019JA027691.
- 766 [34] J. Müller, S. Simon, Y.-C. Wang, U. Motschmann, D. Heyner, J. Schüle,  
767 W.-H. Ip, G. Kleindienst, G. J. Pringle, Origin of Mercury’s double  
768 magnetopause: 3D hybrid simulation study with A.I.K.E.F., *Icarus* 218  
769 (2012) 666–687. doi:10.1016/j.icarus.2011.12.028.
- 770 [35] B. J. Anderson, J. A. Slavin, H. Korth, S. A. Boardsen, T. H. Zurbuchen,  
771 J. M. Raines, G. Gloeckler, R. L. McNutt, S. C. Solomon, The dayside



- 772 magnetospheric boundary layer at Mercury, *Planetary and Space Sci-*  
773 *ence* 59 (2011) 2037–2050. doi:10.1016/j.pss.2011.01.010.
- 774 [36] I. B. Peng, S. Markidis, E. Laure, A. Johlander, A. Vaivads,  
775 Y. Khotyaintsev, P. Henri, G. Lapenta, Kinetic structures of quasi-  
776 perpendicular shocks in global particle-in-cell simulations, *Physics of*  
777 *Plasmas* 22 (2015) 092109. doi:10.1063/1.4930212.
- 778 [37] I. B. Peng, S. Markidis, A. Vaivads, J. Vencels, J. Amaya, A. Divin,  
779 E. Laure, G. Lapenta, The formation of a magnetosphere with implicit  
780 particle-in-cell simulations, *Procedia Computer Science* 51 (2015) 1178 –  
781 1187. doi:<http://dx.doi.org/10.1016/j.procs.2015.05.288>, inter-  
782 national Conference On Computational Science 2015: Computational  
783 Science at the Gates of Nature.
- 784 [38] Y. Chen, G. Toth, X. Jia, J. Slavin, W. Sun, S. Markidis, T. Gombosi,  
785 J. Raines, Studying dawn-dusk asymmetries of Mercury’s magnetotail  
786 using mhd-epic simulations, *Journal of Geophysical Research: Space*  
787 *Physics* (Submitted) (2019).
- 788 [39] T. Mukai, H. Yamakawa, H. Hayakawa, Y. Kasaba, H. Ogawa, Present  
789 status of the bepicolombo/Mercury magnetospheric orbiter, *Advances*  
790 *in Space Research* 38 (2006) 578 – 582. doi:[https://doi.org/10.1016/](https://doi.org/10.1016/j.asr.2005.09.038)  
791 [j.asr.2005.09.038](https://doi.org/10.1016/j.asr.2005.09.038), Mercury, Mars and Saturn.
- 792 [40] A. Milillo, M. Fujimoto, E. Kallio, S. Kameda, F. Leblanc, Y. Narita,  
793 G. Cremonese, H. Laakso, M. Laurenza, S. Massetti, S. McKenna-  
794 Lawlor, A. Mura, R. Nakamura, Y. Omura, D. A. Rothery, K. Seki,

795 M. Storini, P. Wurz, W. Baumjohann, E. J. Bunce, Y. Kasaba, J. Hel-  
796 bert, A. Sprague, Hermean Environment WG members, The Bepi-  
797 Colombo mission: An outstanding tool for investigating the Her-  
798 mean environment, *Planetary and Space Science* 58 (2010) 40–60.  
799 doi:10.1016/j.pss.2008.06.005.

800 [41] A. Milillo, M. Fujimoto, G. Murakami, J. Benkhoff, J. Zender, S. Aizawa,  
801 M. Dósa, L. Griton, D. Heyner, G. Ho, S. M. Imber, X. Jia, T. Karls-  
802 son, R. M. Killen, M. Laurenza, S. T. Lindsay, S. McKenna-Lawlor,  
803 A. Mura, J. M. Raines, D. A. Rothery, N. André, W. Baumjohann,  
804 A. Berezhnoy, P. A. Bourdin, E. J. Bunce, F. Califano, J. Deca, S. deÂ  
805 la Fuente, C. Dong, C. Grava, S. Fatemi, P. Henri, S. L. Ivanovski, B. V.  
806 Jackson, M. James, E. Kallio, Y. Kasaba, E. Kilpua, M. Kobayashi,  
807 B. Langlais, F. Leblanc, C. Lhotka, V. Mangano, A. Martindale, S. Mas-  
808 setti, A. Masters, M. Morooka, Y. Narita, J. S. Oliveira, D. Odstreil,  
809 S. Orsini, M. G. Pelizzo, C. Plainaki, F. Plaschke, F. Sahraoui, K. Seki,  
810 J. A. Slavin, R. Vainio, P. Wurz, S. Barabash, C. M. Carr, D. Delcourt,  
811 K. H. Glassmeier, M. Grand e, M. Hirahara, J. Huovelin, O. Korablev,  
812 H. Kojima, H. Lichtenegger, S. Livi, A. Matsuoka, R. Moissl, M. Moncu-  
813 quet, K. Muinonen, E. Quèmerais, Y. Saito, S. Yagitani, I. Yoshikawa,  
814 J. E. Wahlund, Investigating Mercury’s Environment with the Two-  
815 Spacecraft BepiColombo Mission, *Space Science Reviews* 216 (2020) 93.  
816 doi:10.1007/s11214-020-00712-8.

817 [42] B. J. Anderson, C. L. Johnson, H. Korth, R. M. Winslow, J. E.  
818 Borovsky, M. E. Purucker, J. a. Slavin, S. C. Solomon, M. T. Zuber,

- 819 R. L. McNutt, Low-degree structure in Mercury's planetary magnetic  
820 field, *Journal of Geophysical Research E: Planets* 117 (2012) 1–17.  
821 doi:10.1029/2012JE004159.
- 822 [43] R. Keppens, Z. Meliani, A. J. van Marle, P. Delmont, A. Vlasis, B. van  
823 der Holst, Parallel, grid-adaptive approaches for relativistic hydro and  
824 magnetohydrodynamics, *Journal of Computational Physics* 231 (2012)  
825 718–744. doi:10.1016/j.jcp.2011.01.020.
- 826 [44] C. Xia, J. Teunissen, I. E. Mellah, E. Chané, R. Keppens, MPI-  
827 AMRVAC 2.0 for solar and astrophysical applications, *The Astrophys-  
828 ical Journal Supplement Series* 234 (2018) 30. doi:10.3847/1538-4365/  
829 aaa6c8.
- 830 [45] K. G. Powell, P. L. Roe, T. J. Linde, T. I. Gombosi, D. L. De Zeeuw,  
831 A Solution-Adaptive Upwind Scheme for Ideal Magnetohydrodynamics,  
832 *Journal of Computational Physics* 154 (1999) 284–309. doi:10.1006/  
833 jcp.1999.6299.
- 834 [46] L. Griton, F. Pantellini, Z. Meliani, Three-dimensional magnetohy-  
835 drodynamic simulations of the solar wind interaction with a hyperfast-  
836 rotating uranus, *Journal of Geophysical Research: Space Physics* 123  
837 (2018) 5394–5406. doi:10.1029/2018JA025331.
- 838 [47] M. Yagi, K. Seki, Y. Matsumoto, Development of a magnetohydro-  
839 dynamic simulation code satisfying the solenoidal magnetic field con-  
840 dition, *Computer Physics Communications* 180 (2009) 1550 – 1557.  
841 doi:https://doi.org/10.1016/j.cpc.2009.04.010.

- 842 [48] M. Yagi, K. Seki, Y. Matsumoto, D. C. Delcourt, F. Leblanc, Formation  
843 of a sodium ring in Mercury's magnetosphere, *Journal of Geophysical*  
844 *Research: Space Physics* 115 (2010). doi:10.1029/2009JA015226.
- 845 [49] J. Müller, S. Simon, U. Motschmann, J. Schüle, K.-H. Glaßmeier, G. J.  
846 Pringle, A.i.k.e.f.: Adaptive hybrid model for space plasma simulations,  
847 *Computer Physics Communications* 182 (2011) 946–966. doi:10.1016/  
848 *j.cpc.2010.12.033*.
- 849 [50] J. Müller, S. Simon, Y.-C. Wang, U. Motschmann, D. Heyner, J. Schüle,  
850 W.-H. Ip, G. Kleindienst, G. J. Pringle, Origin of Mercury's double  
851 magnetopause: 3d hybrid simulation study with a.i.k.e.f., *Icarus* 218  
852 (2012) 666 – 687. doi:[https://doi.org/10.1016/j.icarus.2011.12.](https://doi.org/10.1016/j.icarus.2011.12.028)  
853 *028*.
- 854 [51] C. Jacquey, V. Génot, E. Budnik, R. Hitier, M. Bouchemit, M. Gan-  
855 gloff, A. Fedorov, B. Cecconi, N. André, B. Lavraud, C. Harvey,  
856 F. Dériot, D. Heulet, E. Pallier, E. Penou, J. L. Pinçon, AMDA, Auto-  
857 mated Multi-Dataset Analysis: A Web-Based Service Provided by the  
858 CDPP, *Astrophysics and Space Science Proceedings* 11 (2010) 239–247.  
859 doi:10.1007/978-90-481-3499-1\_16.
- 860 [52] V. Génot, C. Jacquey, M. Bouchemit, M. Gangloff, A. Fedorov,  
861 B. Lavraud, N. André, L. Broussillou, C. Harvey, E. Pallier, E. Penou,  
862 E. Budnik, R. Hitier, B. Cecconi, F. Dériot, D. Heulet, J. L. Pinçon,  
863 Space Weather applications with CDPP/AMDA, *Advances in Space*  
864 *Research* 45 (2010) 1145–1155. doi:10.1016/j.asr.2009.11.010.

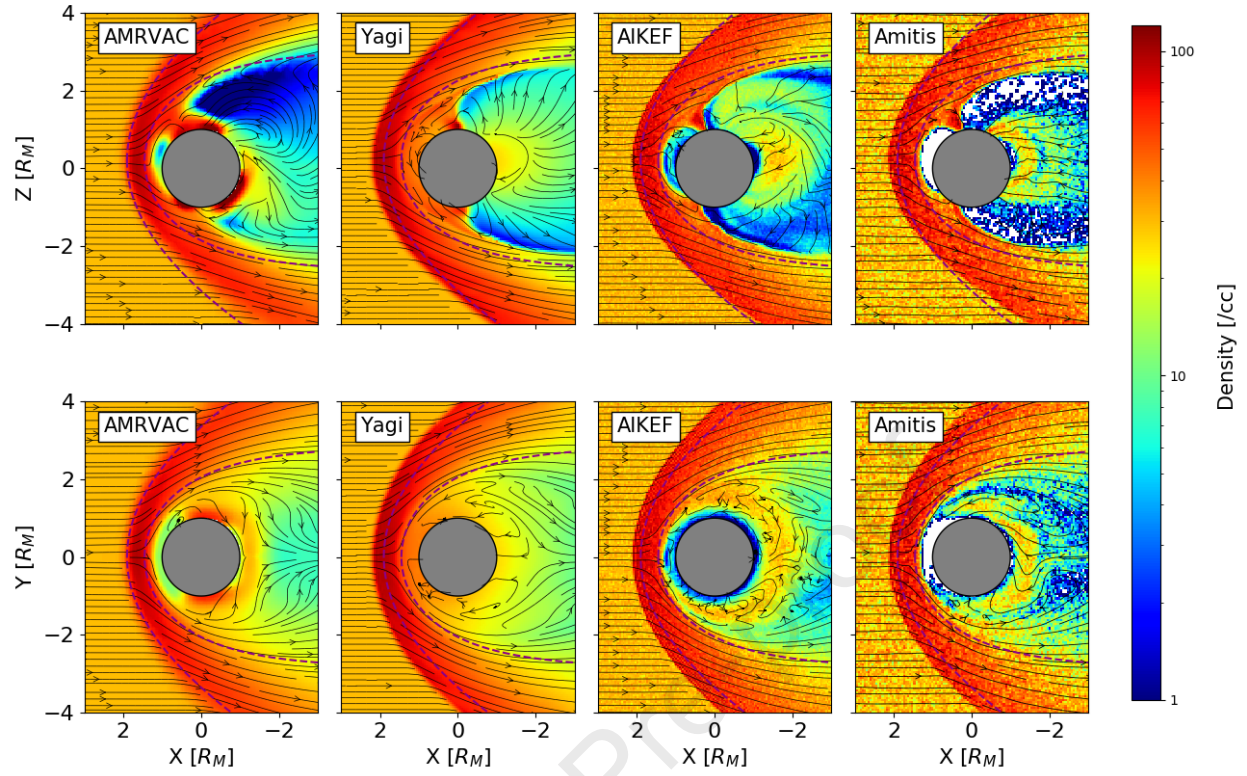
- 865 [53] V. Génot, L. Beigbeder, D. Popescu, N. Dufourg, M. Gangloff, M. Bou-  
866 chemit, S. Caussarieu, J. P. Toniutti, J. Durand, R. Modolo, N. An-  
867 dré, B. Cecconi, C. Jacquy, F. Pitout, A. Rouillard, R. Pinto, S. Er-  
868 ard, N. Jourdane, L. Leclercq, S. Hess, M. Khodachenko, T. Al-Ubaidi,  
869 M. Scherf, E. Budnik, Science data visualization in planetary and helio-  
870 spheric contexts with 3DView, *Planetary and Space Science* 150 (2018)  
871 111–130. doi:10.1016/j.pss.2017.07.007.
- 872 [54] D. A. Roberts, J. Thieman, V. Génot, T. King, M. Gangloff, C. Perry,  
873 C. Wiegand, D. De Zeeuw, S. F. Fung, B. Cecconi, S. Hess, The SPASE  
874 Data Model: A Metadata Standard for Registering, Finding, Accessing,  
875 and Using Heliophysics Data Obtained From Observations and Model-  
876 ing, *Space Weather* 16 (2018) 1899–1911. doi:10.1029/2018SW002038.
- 877 [55] M. Sarantos, P. H. Reiff, T. W. Hill, R. M. Killen, A. L. Urquhart, A  $B_x$ -  
878 interconnected magnetosphere model for Mercury, *Planetary and Space*  
879 *Science* 49 (2001) 1629–1635. doi:10.1016/S0032-0633(01)00100-3.
- 880 [56] E. Marsch, R. Schwenn, H. Rosenbauer, K. H. Muehlhaeuser, W. Pilipp,  
881 F. M. Neubauer, Solar wind protons: Three-dimensional velocity dis-  
882 tributions and derived plasma parameters measured between 0.3 and 1  
883 AU, *Journal of Geophysical Research* 87 (1982) 52–72. doi:10.1029/  
884 JA087iA01p00052.
- 885 [57] M. Sarantos, J. A. Slavin, On the possible formation of alfvén  
886 wings at mercury during encounters with coronal mass ejections,  
887 *Geophysical Research Letters* 36 (2009). URL: <https://agupubs>.

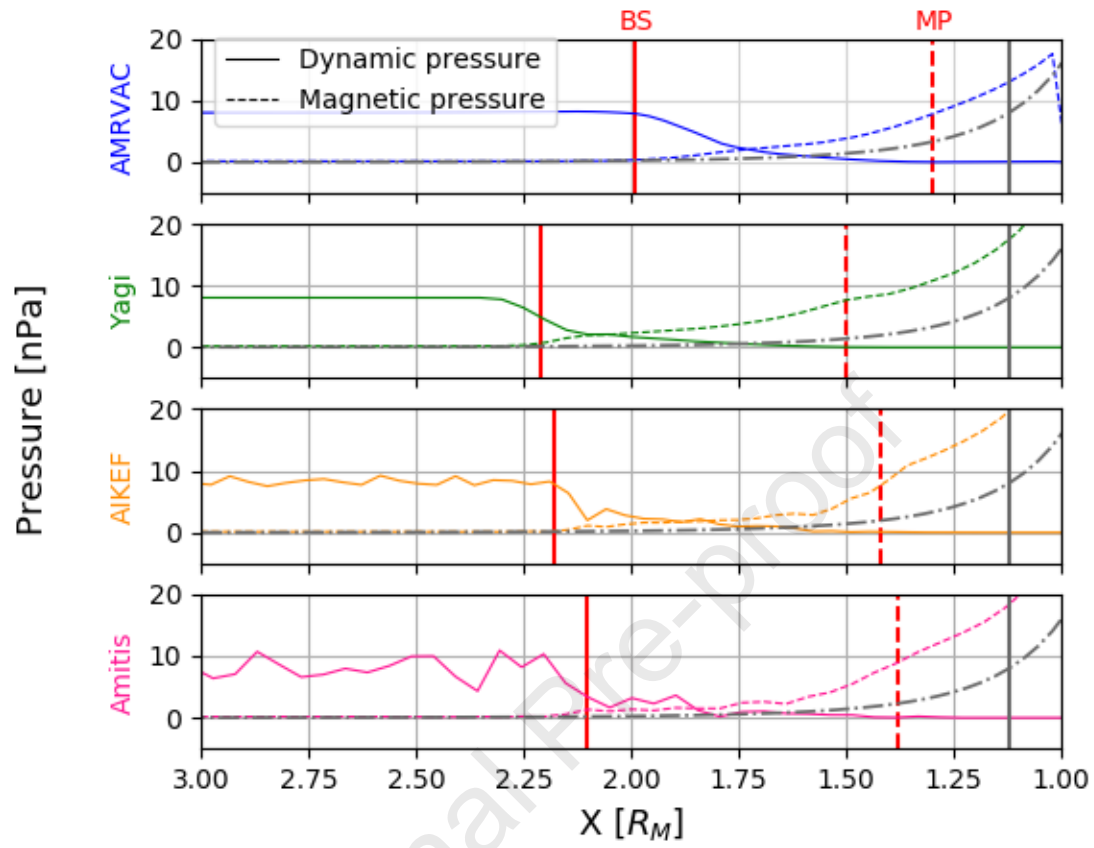
- 888 onlinelibrary.wiley.com/doi/abs/10.1029/2008GL036747. doi:10.  
889 1029/2008GL036747.
- 890 [58] B. J. Anderson, C. L. Johnson, H. Korth, A magnetic disturbance index  
891 for Mercury's magnetic field derived from MESSENGER Magnetome-  
892 ter data, *Geochemistry, Geophysics, Geosystems* 14 (2013) 3875–3886.  
893 doi:10.1002/ggge.20242.
- 894 [59] I. Wilson, Lynn B., M. L. Stevens, J. C. Kasper, K. G. Klein, B. A.  
895 Maruca, S. D. Bale, T. A. Bowen, M. P. Pulupa, C. S. Salem, The  
896 Statistical Properties of Solar Wind Temperature Parameters Near 1  
897 au, *The Astrophysical Journal Supplement Series* 236 (2018) 41. doi:10.  
898 3847/1538-4365/aab71c. arXiv:1802.08585.
- 899 [60] J. A. Slavin, B. J. Anderson, T. H. Zurbuchen, D. N. Baker, S. M.  
900 Krimigis, M. H. Acuña, M. Benna, S. A. Boardsen, G. Gloeckler, R. E.  
901 Gold, G. C. Ho, H. Korth, R. L. McNutt Jr., J. M. Raines, M. Sarantos,  
902 D. Schriver, S. C. Solomon, P. Trávníček, Messenger observations of mer-  
903 cury's magnetosphere during northward imf, *Geophysical Research Let-  
904 ters* 36 (2009). URL: [https://agupubs.onlinelibrary.wiley.com/  
905 doi/abs/10.1029/2008GL036158](https://agupubs.onlinelibrary.wiley.com/doi/abs/10.1029/2008GL036158). doi:10.1029/2008GL036158.
- 906 [61] J. H. Shue, J. K. Chao, H. C. Fu, C. T. Russell, P. Song, K. K. Khurana,  
907 H. J. Singer, A new functional form to study the solar wind control of the  
908 magnetopause size and shape, *Journal of Geophysical Research (Space  
909 Physics)* 102 (1997) 9497–9512. doi:10.1029/97JA00196.
- 910 [62] G. B. Andrews, T. H. Zurbuchen, B. H. Mauk, H. Malcom, L. A. Fisk,

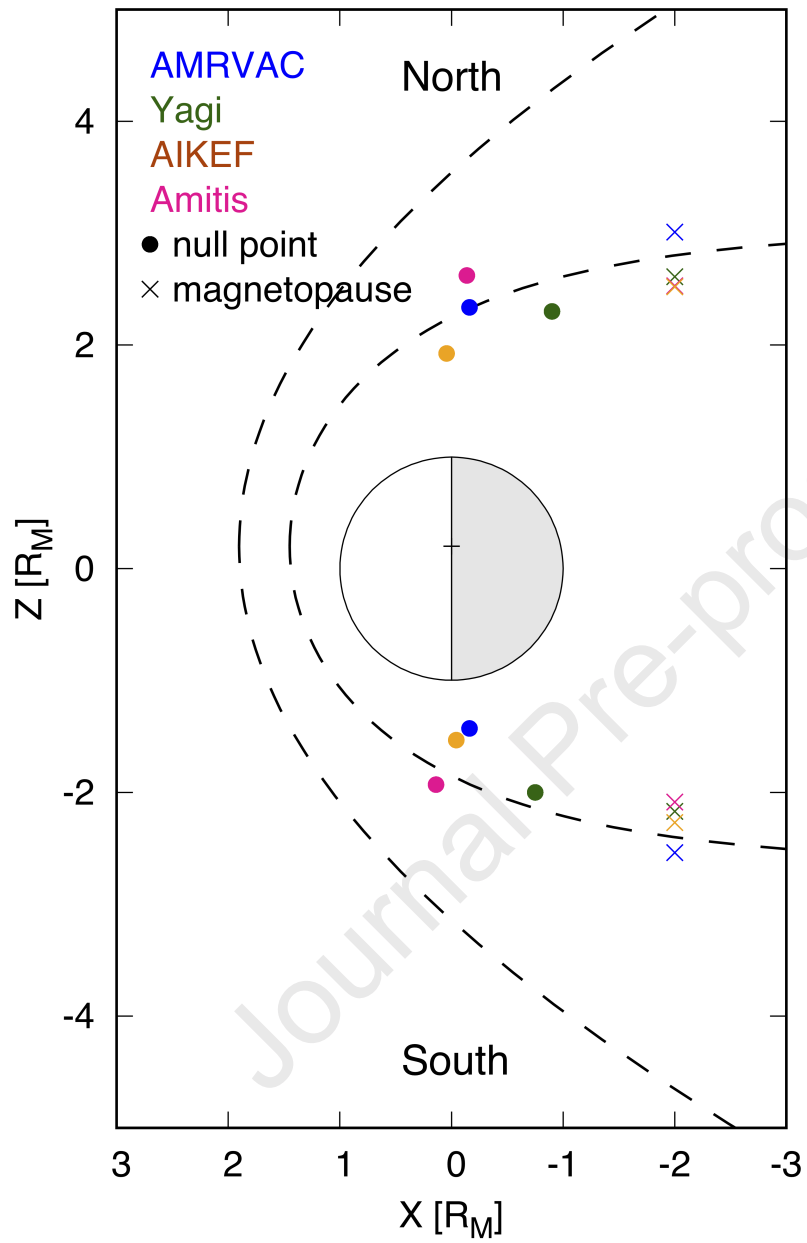
- 911 G. Gloeckler, G. C. Ho, J. S. Kelley, P. L. Koehn, T. W. Lefevre, S. S.  
912 Livi, R. A. Lundgren, J. M. Raines, The Energetic Particle and Plasma  
913 Spectrometer Instrument on the MESSENGER Spacecraft, *Space Sci-*  
914 *ence Reviews* 131 (2007) 523–556. doi:10.1007/s11214-007-9272-5.
- 915 [63] W. Baumjohann, A. Matsuoka, W. Magnes, K.-H. Glassmeier, R. Naka-  
916 mura, H. Biernat, M. Delva, K. Schwingenschuh, T. Zhang, H.-U.  
917 Auster, K.-H. Fornacon, I. Richter, A. Balogh, P. Cargill, C. Carr,  
918 M. Dougherty, T. S. Horbury, E. A. Lucek, F. Tohyama, T. Taka-  
919 hashi, M. Tanaka, T. Nagai, H. Tsunakawa, M. Matsushima, H. Kawano,  
920 A. Yoshikawa, H. Shibuya, T. Nakagawa, M. Hoshino, Y. Tanaka,  
921 R. Kataoka, B. J. Anderson, C. T. Russell, U. Motschmann, M. Shi-  
922 nohara, Magnetic field investigation of Mercury’s magnetosphere and  
923 the inner heliosphere by MMO/MGF, *Planetary and Space Science* 58  
924 (2010) 279–286. doi:10.1016/j.pss.2008.05.019.
- 925 [64] K. H. Glassmeier, H. U. Auster, D. Heyner, K. Okrafka, C. Carr,  
926 G. Berghofer, B. J. Anderson, A. Balogh, W. Baumjohann, P. Cargill,  
927 U. Christensen, M. Delva, M. Dougherty, K. H. Fornacon, T. S. Horbury,  
928 E. A. Lucek, W. Magnes, M. Mandea, A. Matsuoka, M. Matsushima,  
929 U. Motschmann, R. Nakamura, Y. Narita, H. O’Brien, I. Richter,  
930 K. Schwingenschuh, H. Shibuya, J. A. Slavin, C. Sotin, B. Stoll,  
931 H. Tsunakawa, S. Vennerstrom, J. Vogt, T. Zhang, The fluxgate magne-  
932 tometer of the BepiColombo Mercury Planetary Orbiter, *Planetary and*  
933 *Space Science* 58 (2010) 287–299. doi:10.1016/j.pss.2008.06.018.
- 934 [65] Y. Saito, J. Sauvaud, M. Hirahara, S. Barabash, D. Delcourt,

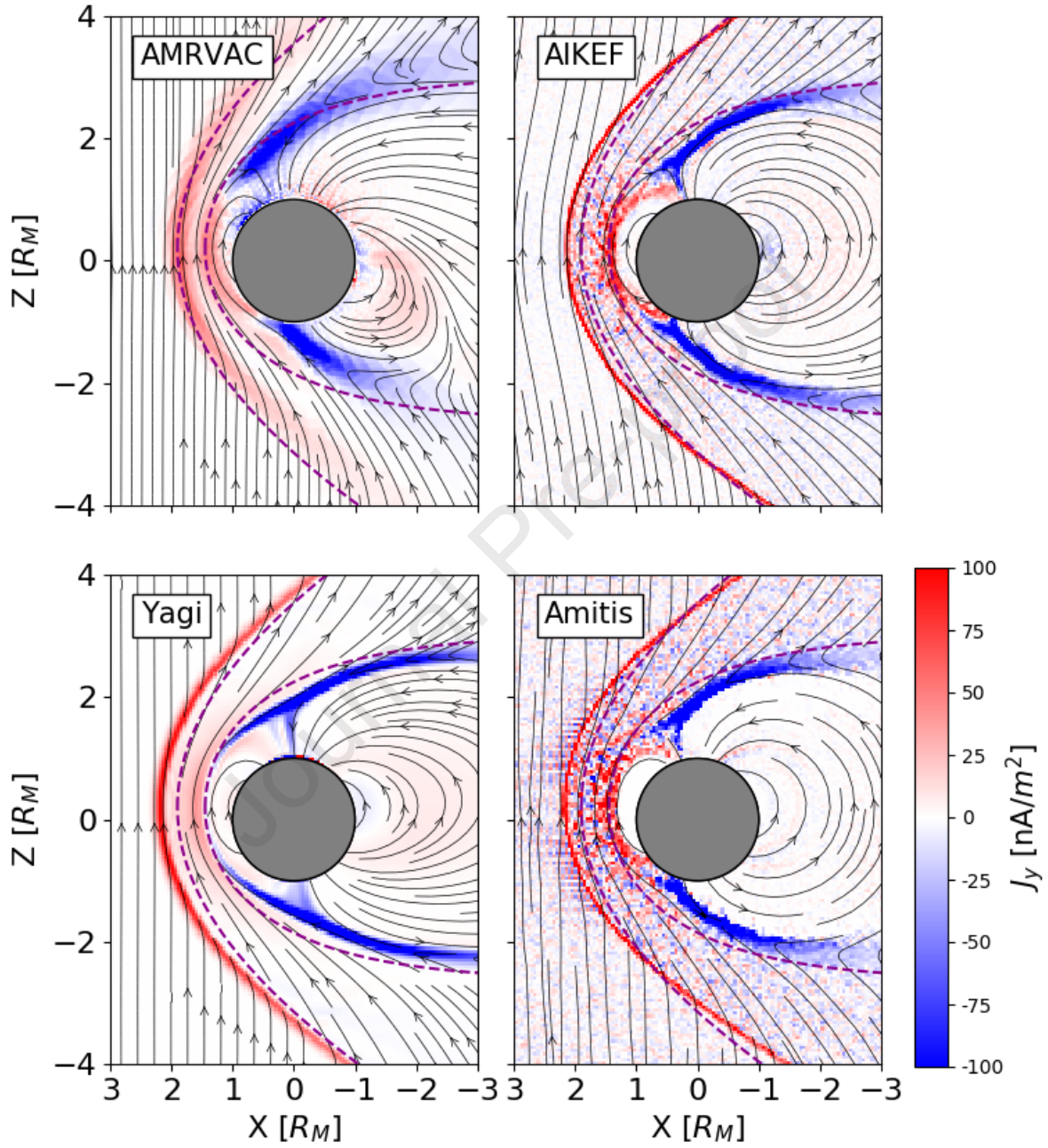
- 935 T. Takashima, K. Asamura, Scientific objectives and instrumentation of  
936 Mercury plasma particle experiment (mppe) onboard mmo, *Planetary*  
937 *and Space Science* 58 (2010) 182 – 200. doi:[https://doi.org/10.1016/  
938 j.pss.2008.06.003](https://doi.org/10.1016/j.pss.2008.06.003), comprehensive Science Investigations of Mercury:  
939 The scientific goals of the joint ESA/JAXA mission BepiColombo.
- 940 [66] Y. Kasaba, J.-L. Bougeret, L. Blomberg, H. Kojima, S. Yagitani,  
941 M. Moncuquet, J.-G. Trotignon, G. Chanteur, A. Kumamoto, Y. Kasa-  
942 hara, J. Lichtenberger, Y. Omura, K. Ishisaka, H. Matsumoto, The  
943 plasma wave investigation (pwi) onboard the bepicolombo/mmo: First  
944 measurement of electric fields, electromagnetic waves, and radio waves  
945 around Mercury, *Planetary and Space Science* 58 (2010) 238 –  
946 278. doi:<https://doi.org/10.1016/j.pss.2008.07.017>, comprehen-  
947 sive Science Investigations of Mercury: The scientific goals of the joint  
948 ESA/JAXA mission BepiColombo.
- 949 [67] S. Orsini, S. Livi, K. Torkar, S. Barabash, A. Milillo, P. Wurz, A. M. di  
950 Lellis, E. Kallio, SERENA Team, SERENA: A suite of four instruments  
951 (ELENA, STROFIO, PICAM and MIPA) on board BepiColombo-MPO  
952 for particle detection in the Hermean environment, *Planetary and Space*  
953 *Science* 58 (2010) 166–181. doi:10.1016/j.pss.2008.09.012.

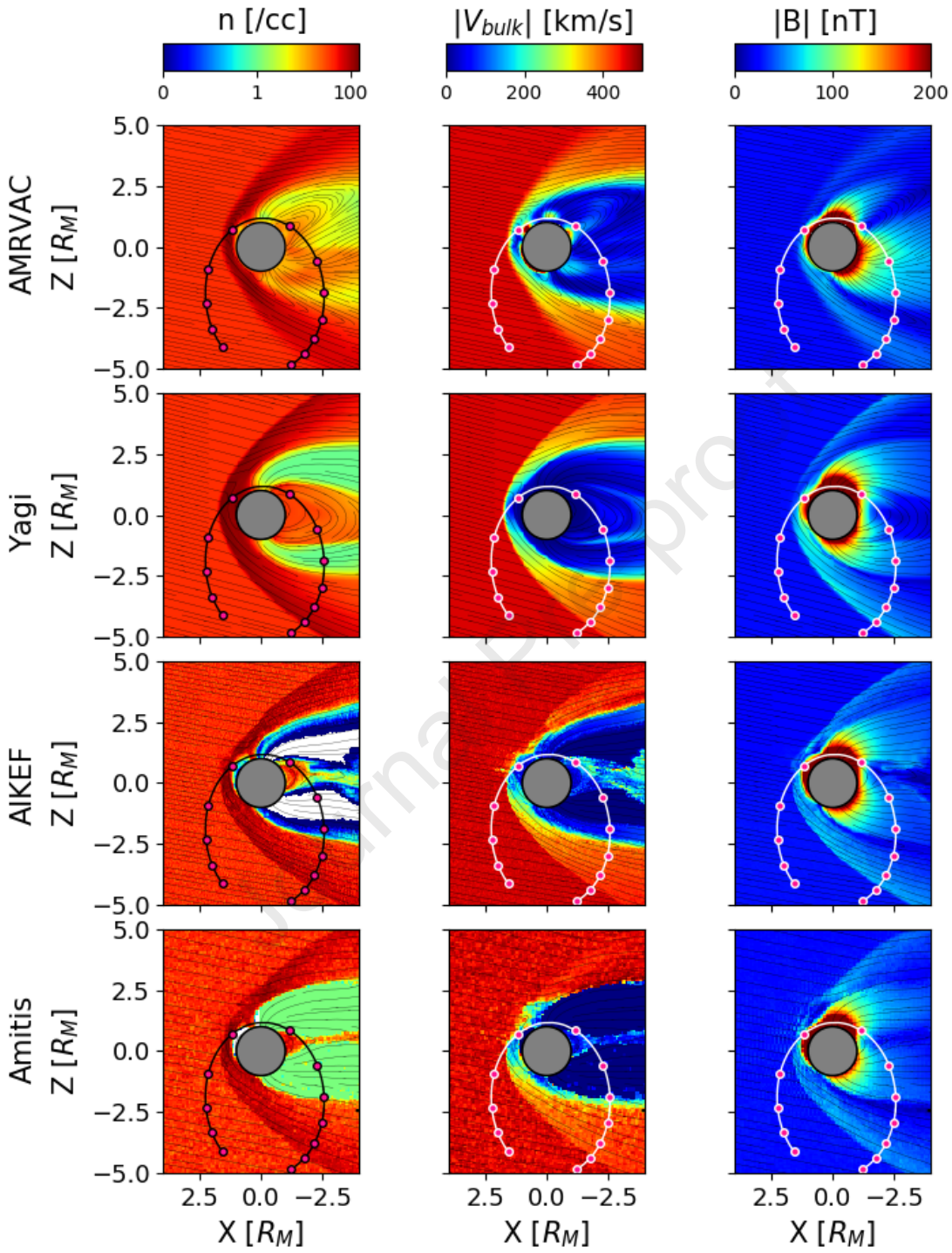


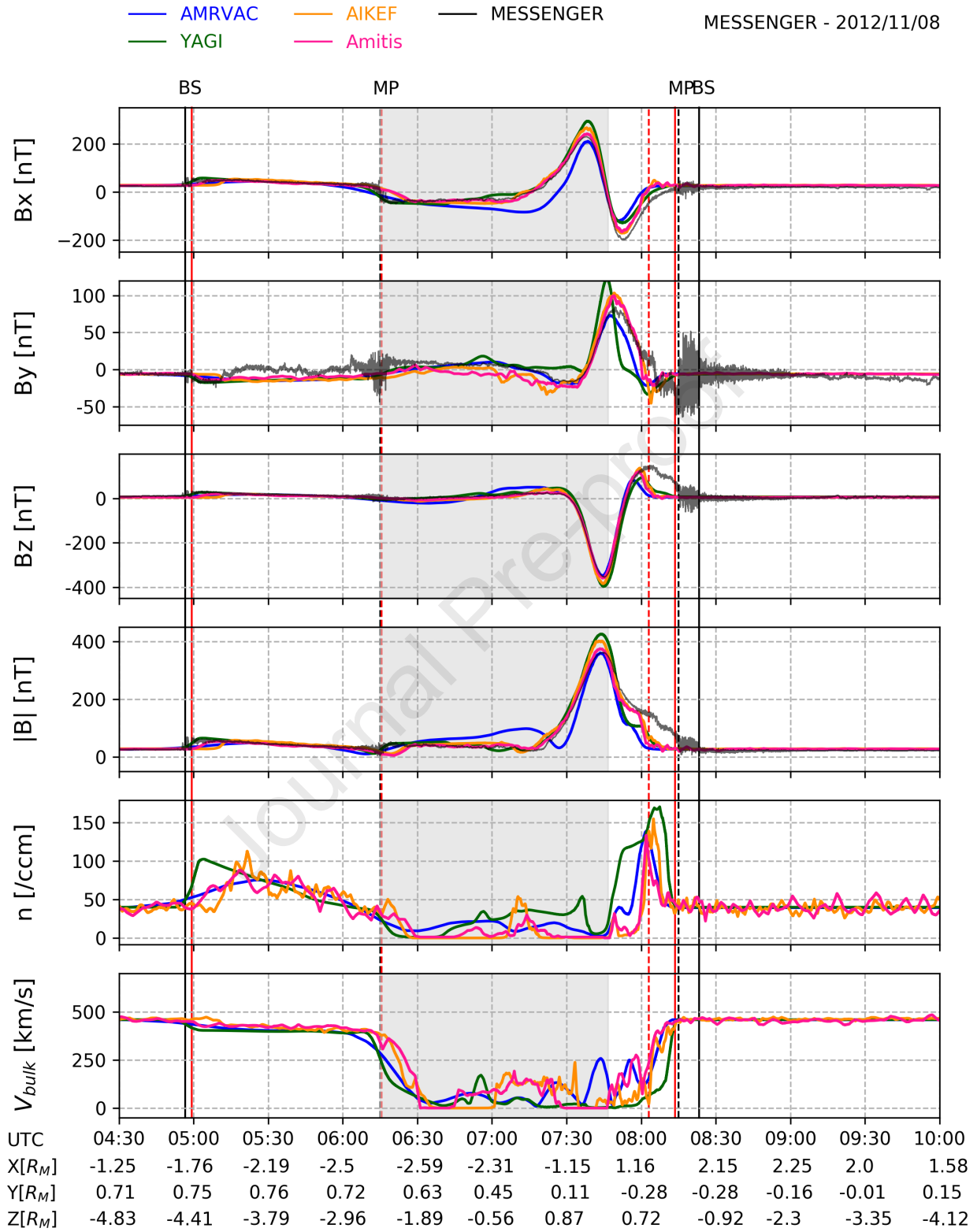


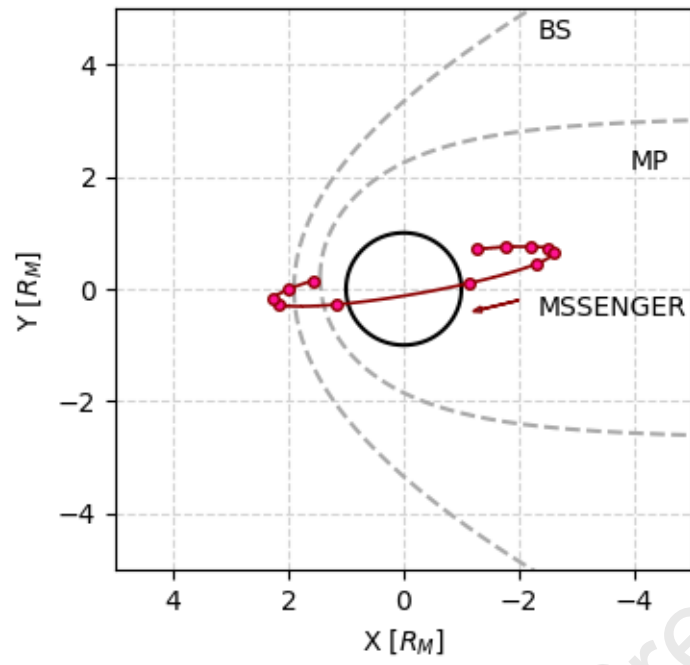


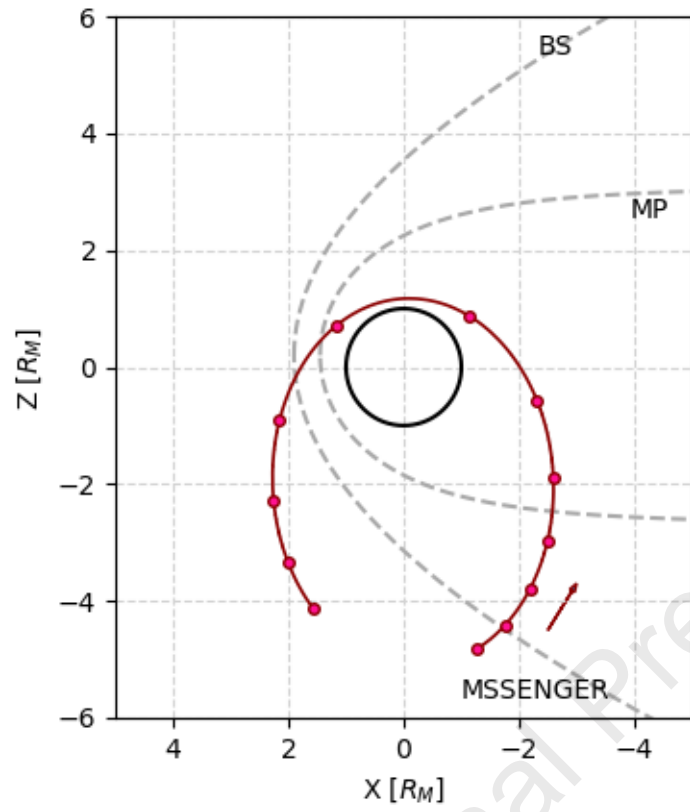






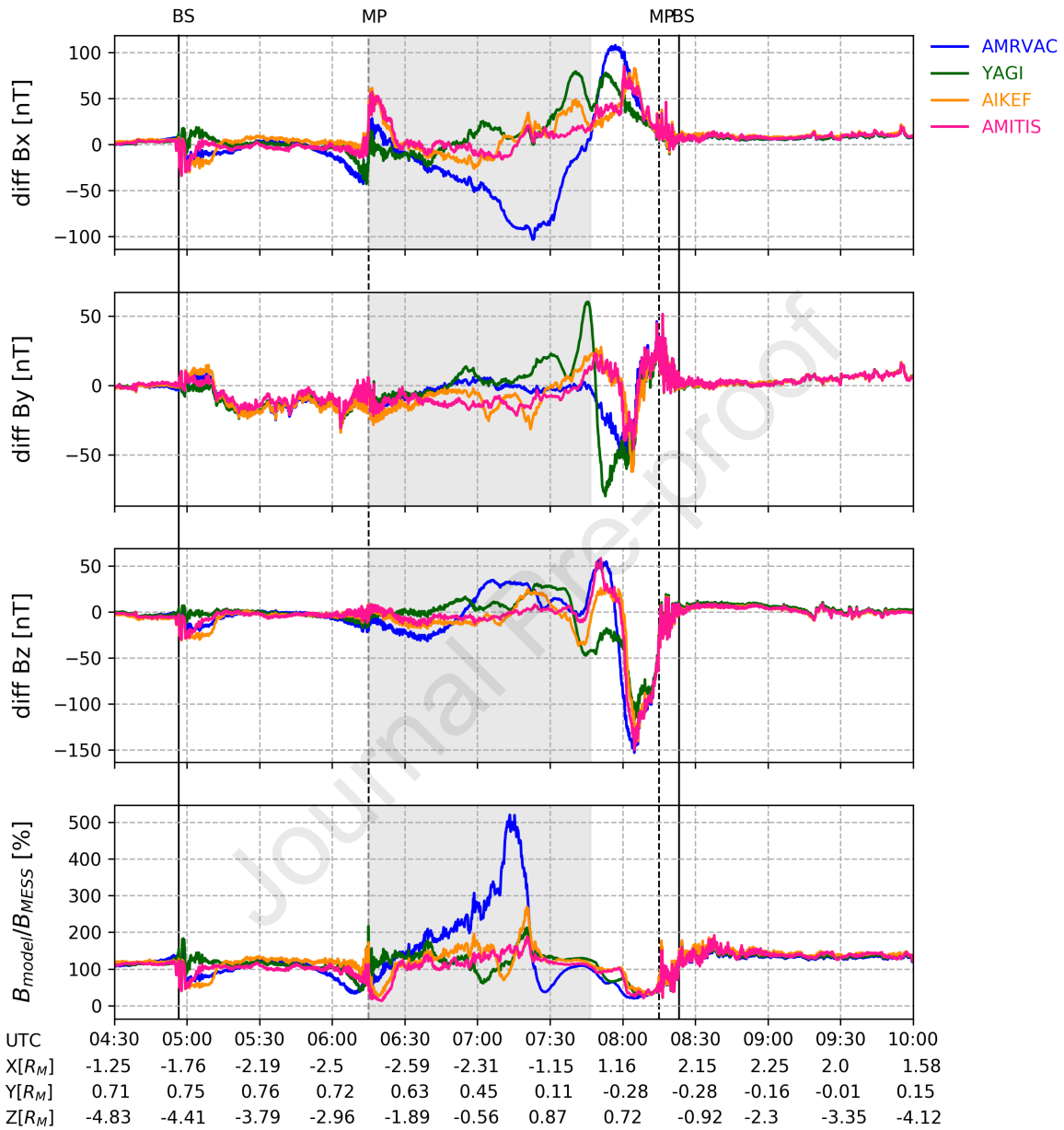




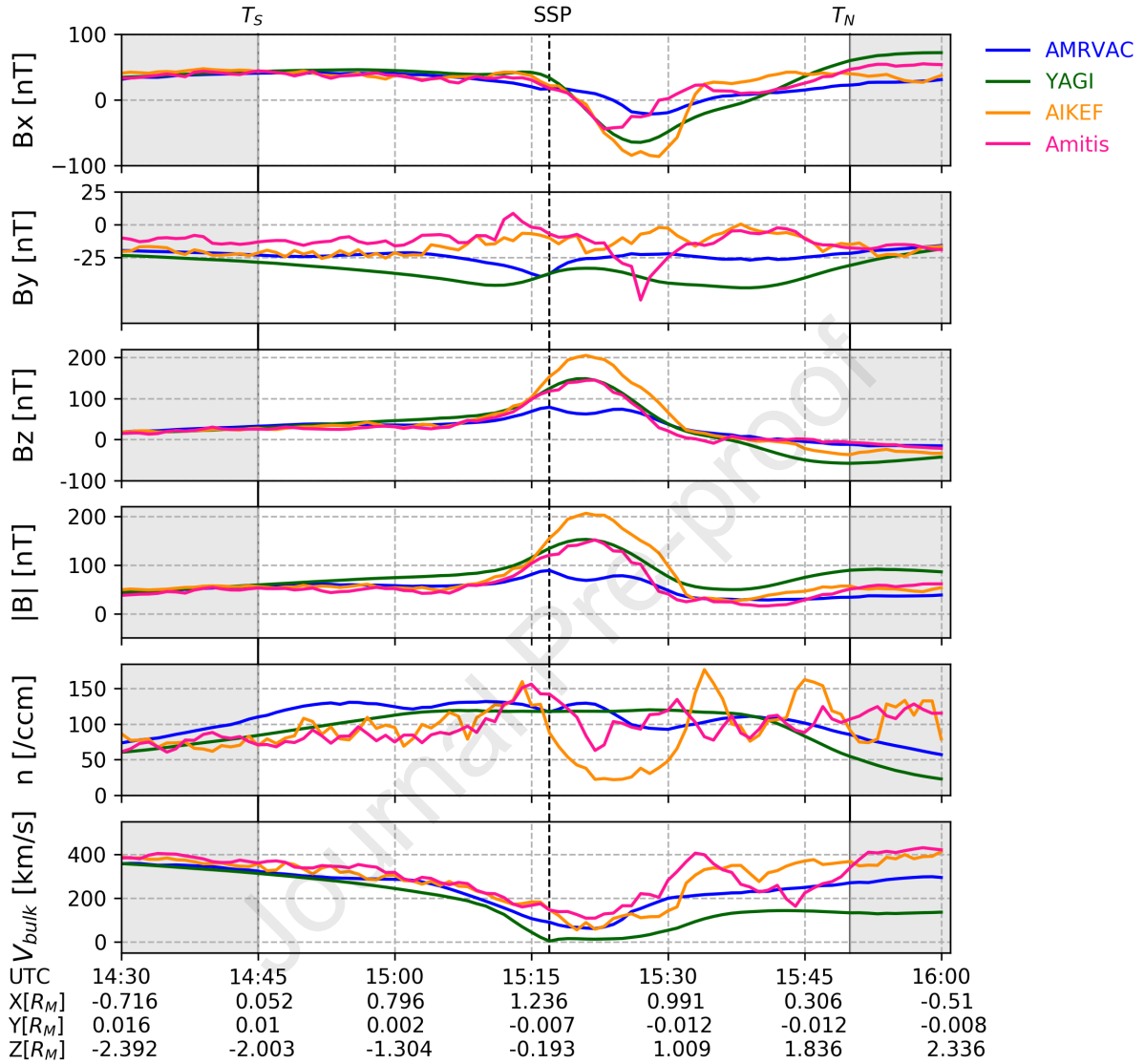


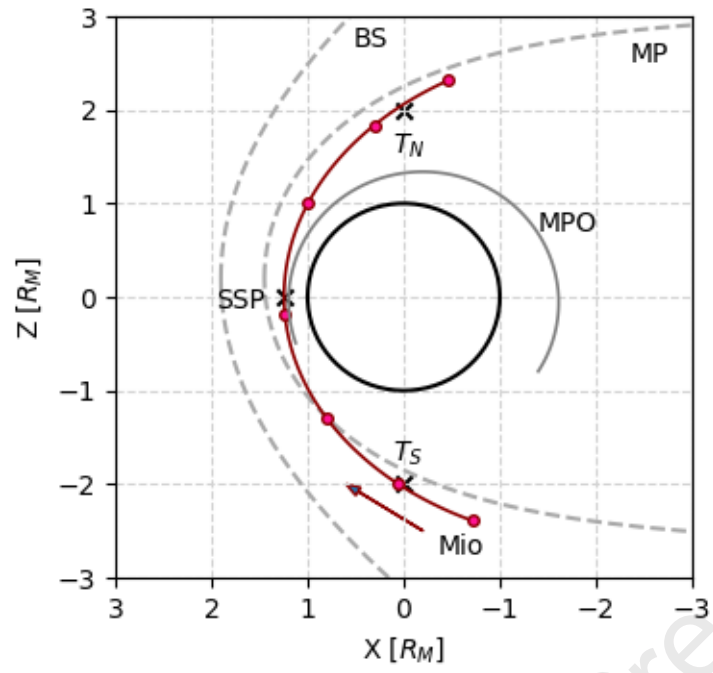


MESSENGER - 2012/11/08

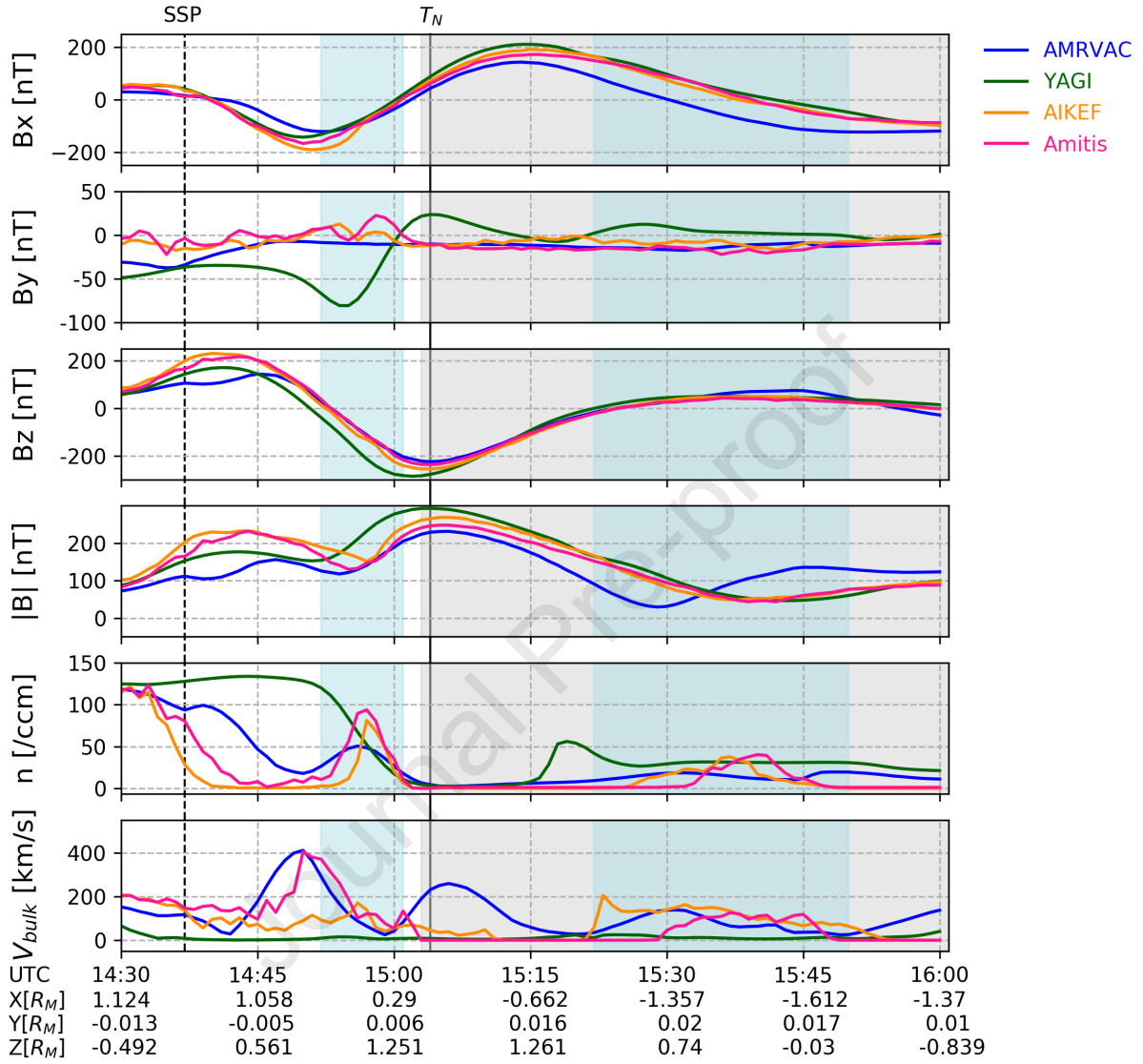


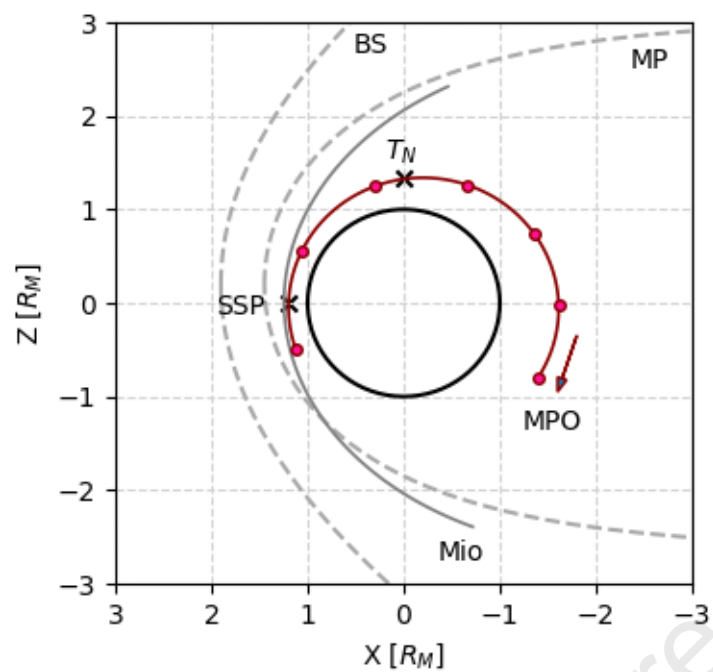
Mio - 2026/04/04





MPO - 2026/04/04





1 **Highlights for the paper :**

2 **Cross-comparison of global simulation models applied to**  
 3 **Mercury's dayside magnetosphere**

4 S. Aizawa<sup>a,b,\*</sup>, L. S. Griton<sup>a,k</sup>, S. Fatemi<sup>c,d</sup>, W. Exner<sup>e,f,g</sup>, J. Deca<sup>h,i,j</sup>, F. Pantellini<sup>k</sup>, M. Yagi<sup>l</sup>, D.  
 5 Heyner<sup>e</sup>, V. Génot<sup>a</sup>, N. André<sup>a</sup>, J. Amaya<sup>m</sup>, G. Murakami<sup>n</sup>, L. Beigbeder<sup>o</sup>, M. Gangloff<sup>a</sup>, M.  
 6 Bouchemit<sup>a</sup>, E. Budnik<sup>p</sup>, H. Usui<sup>q</sup>

7 <sup>a</sup>IRAP, CNRS-CNES-UPS, Toulouse, France

8 <sup>b</sup>Graduate School of Science, Tohoku University, Sendai, Japan

9 <sup>c</sup>Swedish Institute of Space Physics, Kiruna, Sweden

10 <sup>d</sup>Department of Physics at Umeå University, Umeå, Sweden

11 <sup>e</sup>Institute for Geophysics and extraterrestrial Physics, Technische Universität Braunschweig,  
 12 Braunschweig, Germany

13 <sup>f</sup>Institute for Theoretical Physics, Technische Universität Braunschweig, Braunschweig, Germany

14 <sup>g</sup>School of Earth and Atmospheric Sciences, Georgia Institute of Technology, Atlanta, USA

15 <sup>h</sup>Laboratory for Atmospheric and Space Physics (LASP), University of Colorado Boulder, Boulder, Colorado  
 16 80303, USA

17 <sup>i</sup>Institute for Modeling Plasma, Atmospheres and Cosmic Dust, NASA/SSERVI, California 94035, USA

18 <sup>j</sup>Laboratoire Atmosphères, Milieux, Observations Spatiales (LATMOS), Université de Versailles `a Saint  
 19 Quentin, 78280 Guyancourt, France

20 <sup>k</sup>LESIA, Observatoire de Paris, Université PSL, CNRS, Sorbonne Université, Université de Paris, 5 place  
 21 Jules Janssen, 92195 Meudon, France

22 <sup>l</sup>RIKEN, Kobe, Japan

23 <sup>m</sup>CmPA, Mathematics Department, KU Leuven, Belgium

24 <sup>n</sup>ISAS/JAXA, Sagamihara, Japan

25 <sup>o</sup>GFI, Toulouse, France

26 <sup>p</sup>Noveltis, Toulouse, France

27 <sup>q</sup>Kobe University, Kobe, Japan

28

29 **Key Points :**

30 **1) First comparison of multiple global simulations of the solar wind interaction**  
 31 **with Mercury's dayside magnetosphere**

32 **2) The results of four distinct simulation approaches are juxtaposed with**  
 33 **MESSENGER observations**

34 **3) In contrast to the magnetosheath thickness, the simulated shock locations**  
 35 **depends on the inner boundary condition of the model**

**Declaration of interests**

The authors declare that they have no known competing financial interests or personal relationships that could have appeared to influence the work reported in this paper.

The authors declare the following financial interests/personal relationships which may be considered as potential competing interests:

Journal Pre-proof